Exact Multistatic Interferometric Imaging via Generalized Wirtinger Flow

Bariscan Yonel, *Student Member, IEEE*, Il-Young Son, and Birsen Yazici, *Senior Member, IEEE*

***Abstract*—We present a novel, exact method to address the interferometric inversion problem for multistatic wave-based imaging based on Generalized Wirtinger Flow (GWF) [1]. Interferometric imaging is a relative of phase retrieval, which arises from cross-correlating measurements from pairs of receivers. GWF provides a theoretical framework to process scattering data satisfying the Born approximation, and guarantees exact recovery of the underlying scene reflectivity vector from interferometric measurements if the discretized lifted forward model satisfies the restricted isometry property over rank-1, positive semi-definite matrices with a sufficiently small restricted isometry constant (RIC). To this end, we design a linear deterministic discrete lifted forward model for interferometric multistatic radar measurements such that the exact recovery conditions of GWF are satisfied. Our results identify a lower limit on the pixel spacing and the sample complexity for exact multistatic radar imaging. We provide a numerical study of our RIC and pixel spacing bounds on synthetic single scattering data, which show that GWF can achieve exact recovery with super-resolution. While our primary interest lies in radar imaging, our results are applicable to other multistatic wave-based imaging problems such as those arising in acoustics and geophysics.**

***Index Terms*—Multi-static radar, radar imaging, non-convex optimization, interferometric inversion, phase retrieval, wirtinger flow.**

I. Introduction

A. Motivation and Objective

IN THIS paper, we study the exact reconstruction of complex scenes in the context of multistatic interferometric imaging. Interferometric imaging is a close relative of phaseless imaging where, in lieu of self-correlated, intensity only data, we have pairwise cross-correlated data that introduces a phase component. This work establishes *Generalized Wirtinger Flow* (GWF), a computationally efficient interferometric inversion method developed in [1], as a theoretical framework for exact multistatic imaging of arbitrary scenes from scattering data satisfying the Born approximation, while relating its recovery guarantees to the imaging system parameters. To this end, we design a deterministic and underdetermined linear measurement model satisfying the GWF's sufficient condition for exact recovery. In addition, under the single scattering assumption, we show that it is possible to obtain exact reconstruction at a pixel spacing smaller than the resolution limit of Fourier-based methods and provide minimum order of measurements sufficient to guarantee such reconstruction.

The recently developed GWF algorithm is inspired by standard Wirtinger Flow (WF) [2] developed for the generalized phase retrieval problem to overcome practical drawbacks of then state-of-the art lifting based methods [3], [4]. The GWF algorithm extends the standard WF to interferometric inversion problems, and identifies a sufficient condition for exact recovery with arbitrary linear measurement models characterized over the *lifted* domain. Hence, unlike standard WF which guarantees exact recovery for specific random measurement models, GWF theory guarantees exact recovery for a general class of interferometric inversion problems including random and deterministic models that abide by a single condition. In particular, the sufficient condition requires the lifted forward map to satisfy the restricted isometry property (RIP) for rank-1, positive semi-definite (PSD) matrices with a sufficiently small restricted isometry constant (RIC). To the best of our knowledge, our work is the first in which a deterministic and underdetermined forward model satisfying RIP for rank-1, PSD matrices in the lifted domain has been designed.

We provide two outcomes that unify the imaging problem with the abstract theory of GWF. First, we determine the minimum pixel spacing that can satisfy the sufficient condition for exact recovery via the GWF algorithm. Our lower bound depends on the imaging system parameters, thereby, quantifies the range of values and imaging scenarios for exact recovery guarantees to hold. For common radar imaging parameters spanning passive and active imaging modalities, this fundamental lower bound outperforms the range resolution limit of Fourier-based imaging methods for sufficiently small scenes.

Secondly, we determine the sample complexity in the order of the number of unknowns to be reconstructed. Unlike the classical results from electromagnetic scattering theory which study the degrees of freedom of scattered fields via their spatially band-limited nature and Nyquist sampling [5], [6], our analysis is based on the discrete problem, with a geometry consisting of sparsely distributed, static, terrestrial receivers. Furthermore, our sampling complexity result directly relates to the exact recovery guarantees of GWF through the properties of the lifted forward map, rather than the accuracy of interpolating

Manuscript received June 8, 2019; revised October 11, 2019, December 11, 2019, and January 1, 2020; accepted January 3, 2020. Date of publication January 16, 2020; date of current version February 11, 2020. This work was supported in part by the Air Force Office of Scientific Research under Grants FA9550-16-1-0234 and FA9550-19-1-0284, in part by the Office of Naval Research under Grant N0001418-1-2068, and in part by the National Science Foundation under Grant ECCS-1809234. The associate editor coordinating the review of this manuscript and approving it for publication was Dr. Ilaria Catapano. *(Corresponding author: Birsen Yazici.)*

The authors are with the Department of Electrical, Computer and Systems Engineering, Rensselaer Polytechnic Institute, Troy, NY 12180 USA (e-mail: yonelb@rpi.edu; soni@rpi.edu; yazici@ecse.rpi.edu).

Digital Object Identifier 10.1109/TCI.2020.2967151

the sampled scattered field. Notably, we establish that the exact recovery guarantees of GWF hold for a discrete lifted forward model that is underdetermined. Hence, we specify a multistatic measurement model with an optimal order of measurements for interferometric wave-based imaging.

B. Related Work and Advantages of GWF

Interferometric techniques have a rich history in acoustic, geophysical, and electromagnetic wave-based imaging. Cross correlations are frequently deployed as a fundamental formulation for passive modalities [7]–[11], in which the received ambient signal originates from a source of opportunity, such as a wireless communication signal, digital TV signal or FM radio for radar imaging. On the other hand, cross-correlations were proposed for active imaging problems to mitigate the effects of statistical fluctuations in scattering media [12], [13], clutter [14]–[16], and phase errors in the correlated linear transformations [17]–[20]. More recently, inversion from phaseless scattered fields were proposed [21]–[23], to fully eliminate the need of coherent data acquisition in various modalities to cut implementation costs [24], or evade fundamental issues in maintaining phase coherence over long synthetic apertures [25]. Here, we motivate our approach for interferometric multi-static radar imaging via its advantages over several conventional and modern methods in the literature.

1) Passive Radar: A popular method for passive imaging is the time difference of arrival (TDOA) backprojection [7], [9], [26]–[29]. Although they are computationally efficient, TDOA backprojection is based on certain assumptions on the scatterers [7] that are not applicable for realistic scenes and can produce undesirable background artifacts [30].

To mitigate this problem, methods based on lifting have been adapted to the interferometric measurement model for passive imaging [11], [31]. These methods are inspired by the convex semi-definite programming approaches to phase retrieval [3], [4], [32], [33], which reformulate inversion as a low rank matrix recovery (LRMR) problem. Convexification has the added advantage that LRMR is known to have theoretical exact recovery guarantees under certain conditions on the lifted forward map [34]. However, these advantages come at the cost of increasing the dimension of the inverse problem, and hence introduce several limitations. Specifically, as a result of lifting, LRMR suffers from limitations on spatial sampling of the imaging grid due to high computational complexity and demanding memory requirements [1], [11].

GWF is a non-convex optimization approach that operates fully on the original signal domain, thus avoids lifting the problem at implementation and provides computational and memory efficiency over LRMR methods. Unlike TDOA/FDOA backprojection, GWF guarantees exact recovery without additional prior knowledge or limiting assumptionson the scene. Furthermore, the exact recovery guarantees afforded by LRMR [34] require more stringent conditions on the lifted forward map than that of GWF [1].

2) Active Radar: For active imaging, there exists a rich literature of methods on general multistatic geometries involving distributed antennas [35], [36] or arrays [37]. These include time reversal and beamforming [38], [39], subspace methods (MUSIC [37], [40], linear sampling [41]–[43]), and iterative optimization schemes [44]–[46].

Time-reversal, beamforming and MUSIC have wide use in array imaging problems. These methods assume that the scatterers in the scene of interest are point-like and the number of measurements are greater than number of scatterers in the scene [40], [47]. This is in stark contrast to our GWF framework, in which no such assumptions are needed.

Linear sampling methods (LSM) were devised to extend the applicability of subspace methods to the reconstruction of extended targets in the far field and can recover the boundaries of extended objects [41], [42]. Similar to our imaging system geometry, linear sampling methods originally considered a scenario that the receivers and transmitters fully encircle the scene of interest in the far field. The method reportedly degrades when the aperture angle is less than 2π radians [48], which was effectively addressed by using a modified support indicator and multi-frequency data to produce accurate imagery in [49]. More recently in [50], [51] quantitative reconstructions were obtained via LSM by means of incorporating virtual experiments to counter aspect limitations. Notably, our result for multi-static radar measurements captures an analytic dependence on the aperture angle to attain the sufficient condition of GWF on the discrete lifted forward model for exact recovery. Hence, an imaging system can accordingly be designed to guarantee exact recovery via GWF when the aperture angle is limited.

Regularized iterative reconstruction approaches, such as total variation (TV) [44] and ℓ-1 regularization [45], [46], have shown to achieve edge preservation. However, regularized iterative reconstruction approaches, in general, do not offer a theoretical exact recovery guarantee. Notably, TV regularization, while convex, is known to have multiple non-trivial minimizers. In addition, the TV regularizer does not have a closed form proximity operator, hence iterative reconstruction requires an inner optimization problem at each iteration. Similar problems also exist with ℓ_1 regularization due to existence of a tuning parameter, which is heuristically determined. More importantly, the ℓ_1 regularizer is based on sparsity assumptions on the unknown, which may not be applicable to realistic scenes. GWF, on the other hand, offers exact recovery guarantees for complex, realistic scenes under the Born approximation, with low computational complexity per iteration to solve the discretized inverse problem.

C. Organization of the Paper

In Section II, we describe the signal model for interferometric multistatic radar. Section III presents our main results on the relation of imaging system parameters of multistatic radar to the RIC over rank-1 real-valued PSD matrices. Section IV describes the simulated experiments performed with synthetic data generated under the Born approximation to verify our results in Section III. Section V concludes the paper.

II. Signal Model

A. Received Data Model

Let N be the number of receivers each deployed at different spatial locations $\mathbf{a}_i^r, i = 1, \ldots, N$, where subscript i denotes the i-th receiver and superscript r denotes receiver. Assume a single transmitter located at $\mathbf{a}^t$. Furthermore, without loss of generality, we assume that the ground topography is flat. Thus, each spatial location in three-dimensional space is represented as $\mathbf{x} = [\boldsymbol{x}, 0]$ where $\boldsymbol{x} \in \mathbb{R}^2$. Under these assumptions and that only the scattered field is being measured under the Born approximation, the received signal at each receiver for multistatic radar can be modeled as [52]

$$f_i(\omega) = \int_D \mathrm{e}^{\mathrm{i}\omega/c_0\phi_i(\mathbf{x})} A_i(\boldsymbol{x},\omega)\rho(\boldsymbol{x})d\boldsymbol{x}, \quad \omega \in [\omega_c - B/2, \omega_c + B/2] \subset \mathbb{R} \tag{1}$$

where

$$\phi_i(\mathbf{x}) = |\mathbf{x} - \mathbf{a}_i^r| + \left|\mathbf{x} - \mathbf{a}^t\right| \tag{2}$$

is the bistatic phase function, $D \subset \mathbb{R}^2$ is the support of the scene, ω is the fast-time frequency variable, ω_c is the center frequency, B is the bandwidth, c_0 is the speed of light, ρ is the target/scene reflectivity function; and A_i is the amplitude function given by

$$A_i(\mathbf{x},\omega) = \frac{J_i(\mathbf{x},\omega)J_t(\mathbf{x},\omega)}{|\mathbf{x} - \mathbf{a}_i^r|\,|\mathbf{x} - \mathbf{a}^t|} \tag{3}$$

with J_i, and J_t being the receiver and transmitter antenna beampatterns.

B. Correlated Measurements

Given the data model (1), we consider the interferometric data, i.e. fast-time cross-correlation of the measurements at pairs of different receivers. Furthermore, we make the assumption that $|J_t(\mathbf{x},\omega_m)| \approx C_t \in \mathbb{R}^+$. In other words, we assume that the transmitted waveform has a flat spectrum, and that the scene remains in the -3 dB beam-width of the illumination pattern. This is typical of radar waveforms and waveforms of opportunity such as phase shift keying (PSK) modulation found in orthogonal frequency-division multiplexing (OFDM) common among digital communications. Using (1)–(3), the correlated measurements can be modeled as

$$d_{i,j}(\omega) = \int_{D\times D} \mathrm{e}^{\mathrm{i}\omega/c_0\varphi_{i,j}(\mathbf{x},\mathbf{x}')} A_{i,j}(\boldsymbol{x},\boldsymbol{x}',\omega)\tilde{\rho}(\boldsymbol{x},\boldsymbol{x}')d\boldsymbol{x}d\boldsymbol{x}' \tag{4}$$

where

$$\varphi_{i,j}(\mathbf{x},\mathbf{x}') = |\mathbf{x} - \mathbf{a}_i^r| + \left|\mathbf{x} - \mathbf{a}^t\right| - \left|\mathbf{x}' - \mathbf{a}_j^r\right| - \left|\mathbf{x}' - \mathbf{a}^t\right|, \tag{5}$$

$$A_{i,j}(\boldsymbol{x},\boldsymbol{x}',\omega) = A_i(\boldsymbol{x},\omega)A_j^*(\boldsymbol{x}',\omega) \tag{6}$$

and

$$\tilde{\rho}(\boldsymbol{x},\boldsymbol{x}') = \rho(\boldsymbol{x})\rho^*(\boldsymbol{x}') \tag{7}$$

with $(\cdot)^*$ denoting complex conjugation. We call $\tilde{\rho}$ the lifted version of ρ or the *Kronecker scene*.

We next make the small-scene and far-field approximation and approximate the phase term in (5) as

$$\varphi_{i,j}(\mathbf{x},\mathbf{x}') \approx |\mathbf{a}_i^r| - \left|\mathbf{a}_j^r\right| - \langle\hat{\mathbf{a}}_i^r,\mathbf{x}\rangle + \langle\hat{\mathbf{a}}_j^r,\mathbf{x}'\rangle - \langle\hat{\mathbf{a}}^t,\mathbf{x}-\mathbf{x}'\rangle \tag{8}$$

where $\hat{\mathbf{a}}$ is the unit vector in the direction of $\mathbf{a}$, and (6) as

$$A_{i,j}(\boldsymbol{x},\boldsymbol{x}',\omega) \approx \alpha_{i,j} := \frac{C_t^2 J_i(\boldsymbol{x}_o,\omega)J_j(\boldsymbol{x}_o,\omega)^*}{|\mathbf{a}_i^r|\,\left|\mathbf{a}_j^r\right|\,|\mathbf{a}^t|^2} \tag{9}$$

where $\boldsymbol{x}_o$ denotes the center of the scene, with $|J_i(\boldsymbol{x}_o,\omega)| \approx C_i$ over the observed frequency band. We assume that the support of the scene is discretized into K discrete spatial points, $\{\boldsymbol{x}_k |\, k = 1,\ldots,K\}$ and define $\boldsymbol{\rho} = [\rho(\boldsymbol{x}_1),\ldots,\rho(\boldsymbol{x}_K)]^T$. We further assume that the support of ω is discretized into M samples, $\Omega = \{\omega_m | m = 1,\ldots,M\}$ so that $\boldsymbol{d}_{i,j} = [d_{i,j}(\omega_1),\ldots,d_{i,j}(\omega_M)]^T$, $\omega_m = \omega_c - B/2 + \frac{m-1}{M}B$.

We write (4) as

$$d_{i,j}(\omega_m) = \langle\mathbf{L}_i^m,\boldsymbol{\rho}\rangle\langle\mathbf{L}_j^m,\boldsymbol{\rho}\rangle^* = \mathrm{tr}\left(\mathbf{L}_j^m(\mathbf{L}_i^m)^H\tilde{\boldsymbol{\rho}}\right) \tag{10}$$

where

$$\mathbf{L}_i^m = [\mathrm{e}^{-\mathrm{i}\omega_m/c_0\phi_i(\mathbf{x}_k)}A_i]_{k=1}^K, \qquad i = 1,\ldots N. \tag{11}$$

Let

$$\mathbf{d} = \frac{1}{\sqrt{M\binom{N}{2}}}[\boldsymbol{d}_{1,2}^T,\ldots,\boldsymbol{d}_{N-1,N}^T]^T \tag{12}$$

be the full vectorized data scaled by the number of correlated measurements. (10) shows that the data vector $\mathbf{d}$ is linear in $\tilde{\boldsymbol{\rho}}$, the Kronecker scene, while it is non-linear in $\boldsymbol{\rho}$. Thus, the data vector can be written as

$$\mathbf{d} = \mathcal{F}(\tilde{\boldsymbol{\rho}}) \tag{13}$$

where $\mathcal{F}$ is a linear mapping from $\mathbb{R}^{K\times K}$ to $\mathbb{C}^{M\binom{N}{2}}$. Alternatively, if $\overline{\boldsymbol{\rho}}$ is the column-wise vectorization of $\tilde{\boldsymbol{\rho}}$,

$$\mathbf{d} = \mathbf{F}\overline{\boldsymbol{\rho}} \tag{14}$$

where $\mathbf{F}$ is a complex-valued matrix of size $M\binom{N}{2} \times K^2$, whose rows are formed by row-wise vectorization of the matrix $\mathbf{L}_i^m(\mathbf{L}_j^m)^H$.

III. Exact Multistatic Wave-Based Imaging

In this section, we are concerned with identifying the imaging system parameters, i.e., design of the measurement vectors $\mathbf{L}_i^m$, $i = 1,\ldots,N$, $m = 1,\ldots,M$, so that the lifted forward map $\mathcal{F}$ satisfies the sufficient condition proved in [1] for exact recovery via the GWF algorithm. We establish all the results presented in this section under the following assumption.

Assumption 1: Let

$$\Phi_{i,j}^{k,k',l,l'} = \langle\hat{\mathbf{a}}_i^r,\mathbf{x}_k - \mathbf{x}_{k'}\rangle - \langle\hat{\mathbf{a}}_j^r,\mathbf{x}_l - \mathbf{x}_{l'}\rangle + \langle\hat{\mathbf{a}}^t,\mathbf{x}_k - \mathbf{x}_{k'} - \mathbf{x}_l + \mathbf{x}_{l'}\rangle. \tag{15}$$

Then, we assume that $\frac{B}{2Mc_0}\Phi_{i,j}^{k,k',l,l'} \ll 2\pi$ for all (i,j,k,k',l,l') where B is the bandwidth of the received signal, M is the number of frequency samples, and c_0 is the speed of light in a vacuum.

Assumption 1 is used to make small angle approximation in the proof of Lemma 1 below. This assumption implies that the number of frequency samples needed depends on the bandwidth of the transmitted waveform and the maximum value of $\Phi_{i,j}^{k,k',l,l'}$, which depends on the size of the scene and the placement of the receivers. As later seen in (25), this assumption is easily satisfied if the scene is sufficiently small.

We next introduce the following lemma that expresses the kernel of the operator $\mathcal{F}$ in terms of sinc functions. This lemma is used in proving Propositions 1 and 2, and for the main result in Theorem 1.

Lemma 1: Suppose Assumption 1 holds. Then, the 2-norm of the data, $\mathbf{d}$ can be written as

$$\|\mathbf{d}\|_2^2 = \|\mathcal{F}\tilde{\boldsymbol{\rho}}\|_2^2 = \frac{\sum_{i<j}|\alpha_{i,j}|^2}{\binom{N}{2}}\left(\|\tilde{\boldsymbol{\rho}}\|_F^2 + \sum_{k\neq k',l\neq l'}\mathcal{K}(\Phi_{i,j}^{k,k',l,l'}) \times \tilde{\rho}(\boldsymbol{x}_k,\boldsymbol{x}_{k'})\tilde{\rho}(\boldsymbol{x}_{l'},\boldsymbol{x}_l)\right) \tag{16}$$

where the phase term $\Phi_{i,j}^{k,k',l,l'}$ is as in (15) and

$$\mathcal{K}(\Phi) = \frac{\sin\left[\left(\omega_c' + \frac{B}{2}\right)\frac{\Phi}{c_0}\right] - \sin\left[\left(\omega_c' - \frac{B}{2}\right)\frac{\Phi}{c_0}\right]}{B\frac{\Phi}{c_0}}, \tag{17}$$

with $\omega_c' = \omega_c - \frac{B}{2M}$.

Proof: See Appendix A. ■

A. GWF Framework for Interferometric Imaging

For establishing the GWF as an exact interferometric wave-based imaging framework, we study the restricted isometry property (RIP) of the lifted forward map $\mathcal{F}$ over the set of rank-1, PSD matrices.

Definition 1: Let $\mathcal{F}: \mathbb{C}^{K\times K} \to \mathbb{C}^{M\binom{N}{2}}$ denote the lifted forward model provided in (13). Then $\mathcal{F}$ satisfies the restricted isometry property over rank-1, positive semi-definite matrices of the form $\tilde{\boldsymbol{\rho}} = \boldsymbol{\rho}\boldsymbol{\rho}^H$, with a restricted isometry constant (RIC)-δ, if

$$(1-\delta)\|\tilde{\boldsymbol{\rho}}\|_F^2 \leq \frac{1}{M}\|\mathcal{F}(\tilde{\boldsymbol{\rho}})\|^2 \leq (1+\delta)\|\tilde{\boldsymbol{\rho}}\|_F^2, \tag{18}$$

for any $\boldsymbol{\rho} \in \mathbb{C}^K$, where $\|\cdot\|_F$ denotes the Frobenius norm.

Notably, we consider a domain of $\boldsymbol{\rho} \in \mathbb{R}^K$ in optimization via GWF, for which the exact recovery guarantees of [1] directly apply. Thereby, the GWF algorithm for interferometric imaging is summarized as follows:

- *Inputs:* Interferometric measurements $d_{ij}(\omega_m)$ and measurement vectors $\mathbf{L}_i^m$, $i = 1, \cdots N$.
- *Initialization: Backproject* the interferometric measurements to the lifted domain, i.e., form an estimator for the Kronecker scene as:

$$\hat{\mathbf{X}} = \frac{1}{M}\mathcal{P}_S\left(\mathrm{Re}\{\mathcal{F}^H(\mathbf{d})\}\right), \tag{19}$$

  and keep its rank-1 approximation $\lambda_0\boldsymbol{\rho}_0\boldsymbol{\rho}_0^H$, where $\mathcal{P}_S$ is the projection operator onto the set of symmetric matrices. The initialization step consists of the outer product of the two measurement vectors for each of the M samples, resulting in $\mathcal{O}(MK^2)$ multiplications, followed by an eigenvalue decomposition with $\mathcal{O}(K^3)$ complexity.
- *Iterations:* Initializing with $\boldsymbol{\rho}_0$, perform gradient descent updates as $\boldsymbol{\rho}_{k+1} = \boldsymbol{\rho}_k - \frac{\mu_k}{\|\boldsymbol{\rho}_0\|^2}\nabla\mathcal{J}(\boldsymbol{\rho}_k)$, having

$$\mathcal{J}(\boldsymbol{\rho}) = \frac{1}{2}\|\mathcal{F}(\boldsymbol{\rho}\boldsymbol{\rho}^H) - \mathbf{d}\|_2^2, \tag{20}$$

  which yields

$$\nabla\mathcal{J}(\boldsymbol{\rho}_k) = \frac{1}{M}\mathcal{P}_S\left(\mathrm{Re}\{\mathcal{F}^H(\mathbf{e}_k)\}\right)\boldsymbol{\rho}_k, \tag{21}$$

  where $(\mathbf{e}_k)_{ij}^m = ((\mathbf{L}_i^m)^H\boldsymbol{\rho}_k\boldsymbol{\rho}_k^H\mathbf{L}_j^m - d_{ij}(\omega_m))$, $\forall i \neq j$, $m = 1, \ldots, M$.

  Each iteration requires the following operations:
  1) Computing and storing the linear terms $(\mathbf{L}_{i,j}^m)^H\boldsymbol{\rho}_k$, requiring M number of K multiplications for each, resulting in $\mathcal{O}(MK)$ multiplications.
  2) Computing the error by cross correlating linear terms, requiring $\mathcal{O}(M)$ multiplications.
  3) Multiplication of the linear terms $(\mathbf{L}_{i,j}^m)^H\boldsymbol{\rho}_k$ and the error e_{ij}^m for each $m = 1, \ldots M$, requiring $\mathcal{O}(M)$ multiplications.
  4) Multiplication of the result in 3 with vectors $\{\mathbf{L}_i^m\}_{m=1}^M$ and $\{\mathbf{L}_j^m\}_{m=1}^M$, requiring $\mathcal{O}(MK)$ multiplications.

  These operations result in $\mathcal{O}(MK)$ multiplications for each iteration.

In particular, [1] establishes that exact recovery of a ground truth $\boldsymbol{\rho}_t \in \mathbb{C}^K$ is guaranteed upto a global phase factor, if the forward operator for the lifted Kronecker scene, satisfies the RIP over the set of rank-1, PSD matrices (i.e., $\tilde{\boldsymbol{\rho}}$) with RIC of less than 0.214. Furthermore, starting from the initial estimate computed from (19), gradient descent iterations minimizing (20) using (21) converges geometrically to the true solution at a rate $1-\kappa$, where κ is upper bounded by

$$\frac{2\mu}{\alpha} \leq \frac{(1-\delta_1)h^2(\delta_1)}{(1+\delta_1)c^2(\delta_1)}, \tag{22}$$

where $h \leq c$ are positive constants solely depending on δ [1].

B. Asymptotic Result

As a stepping stone for our main result, we begin by showing the asymptotic isometry of $\mathcal{F}$ defined in (13), as $\omega_c \to \infty$ and $N \to \infty$. Following our asymptotic analysis of the kernel of $\mathcal{F}$, we characterize its RIP over rank-1, PSD matrices in the non-asymptotic regime. As a result of our non-asymptotic analysis, we derive an upper bound on the restricted isometry constant that is controlled by the imaging system parameters.

Despite its limited use in practice, our initial asymptotic result offers a valuable benchmark for the non-asymptotic case. Notably, it justifies assessing how the isometry of $\mathcal{F}$ is perturbed over the set of rank-1, PSD matrices when the central frequency ω_c, and the number of receivers N are finite. We specifically make use of this perspective in establishing our main result, by analytically evaluating elements $\boldsymbol{\rho}\boldsymbol{\rho}^H$ in the range of $\mathcal{F}^H\mathcal{F}$. Furthermore, it characterizes the expected limiting behavior of our upper bound estimate on the RIC-δ.

The following proposition shows that in the asymptotic regime, i.e., as ω_c gets large, $\mathcal{F}$ becomes a delta function with respect to the phase term $\Phi_{i,j}^{k,k',l,l'}$.

Proposition 1: Under Assumption 1, we have

$$\lim_{\omega_c' \to \infty} \mathcal{K}(\Phi_{i,j}^{k,k',l,l'}) = \begin{cases} 0 & \Phi_{i,j}^{k,k',l,l'} \neq 0 \\ 1 & \Phi_{i,j}^{k,k',l,l'} = 0. \end{cases} \tag{23}$$

Proof: See Appendix B. ■

Given Proposition 1, the next proposition shows that in the limit as $\omega_c \to \infty$ and $N \to \infty$, $\mathcal{F}$ is an isometry.

Proposition 2 (Asymptotic Isometry of $\mathcal{F}$ for large ω_c and N): Under Assumption 1, we have

$$\begin{aligned} \lim_{\omega_c' \to \infty, S \to \infty} & \frac{1}{\binom{N}{2}} \sum_{i<j} |\alpha_{i,j}|^2 W_{i,j} \\ &= \frac{1}{\binom{N}{2}} \sum_{i<j} |\alpha_{i,j}|^2 \sum_{k \neq k', l \neq l'} \mathcal{K}(\Phi_{i,j}^{k,k',l,l'}) \\ &\quad \times \tilde{\rho}(\boldsymbol{x}_k, \boldsymbol{x}_{k'}) \tilde{\rho}(\boldsymbol{x}_{l'}, \boldsymbol{x}_l) = 0 \end{aligned} \tag{24}$$

Proof: See Appendix C. ■

Since in the asymptotic regime $\mathcal{F}$ is an isometry, we can deduce that the RIC over rank-1, PSD should become small as ω_c and N get large. This motivates us to find an upper bound on the rank-1, PSD RIC constant in the non-asymptotic regime in terms of the imaging parameters. In the next subsection, we establish this upper bound.

C. Non-Asymptotic Result

Before we introduce our main theorem, we introduce two further assumptions.

Assumption 2: The scene is enclosed by a square with side L and sampled regularly on a square grid. The coordinate system is centered at the middle of the square. Hence, $\boldsymbol{x} = [x_1, x_2]^T \in [-L/2, L/2] \times [-L/2, L/2]$ with $\sqrt{K}$ samples in both x_1- and x_2-axis and $L = \sqrt{K}\Delta$ where Δ is the pixel spacing.

Under Assumption 2, it is easy to see that the phase term $|\Phi_{i,j}^{k,k',l,l'}|$ is upper bounded by $4L\sqrt{2}$ for any selection of i, j, k, k', l, l'. Then, for Assumption 1, letting $\Delta_{\text{res}} = 2\pi \frac{c_0}{2B}$ be the range resolution given by the Fourier-based methods the small angle approximation holds to high accuracy if

$$M \geq \mathcal{O}\left(\frac{L}{\Delta_{\text{res}}}\right), \tag{25}$$

since $\max_{i,j,k,k',l,l'} |\Phi_{i,j}^{k,k',l,l'}| = \mathcal{O}(L)$. For instance, $M \geq 5.8 \frac{L}{\Delta_{\text{res}}}$ corresponds to a $< 1\%$ error for the sinc approximations in Lemma 1.

Assumption 3:

1) The receivers are isotropic and lie on a circular arc equidistant from each other and to the center of the coordinate system. Let $A \in (0, 2\pi]$ be the aperture of the multistatic system. Then, the azimuth angles of the look-directions are multiples of A/N.
2) All receivers and the transmitter are located at the same height. Let ϕ be the elevation angle in radians. Then, $\hat{\mathbf{a}}_i^r = [\cos\phi\cos\theta_i, \cos\phi\sin\theta_i, \sin\phi]$ where $\theta_i = \frac{Ai}{N}$, $i = 0, \ldots, N-1$ are the azimuth angles of the receivers' look-directions.
3) The transmitter is located on the x_1-axis. Hence, $\hat{\mathbf{a}}_t = [\cos\phi, 0, \sin\phi]^T$.

Assumption 3 allows us to make integral approximation to a Riemann sum in the proof of Theorem 1 (see Appendix D). The approximation error is then incorporated into the result of Theorem 1. Note that the assumption on the location of the transmitter is not essential, but is there for convenience.

We now state our non-asymptotic result in the following theorem, which establishes an upper bound on the rank-1, PSD RIC for the data model presented in (13), in terms of the underlying imaging parameters.

Theorem 1 (RIC of the Lifted Forward Mapping of Multistatic Imaging): Let

$$\lambda_c = \frac{2\pi c_0}{\omega_c'} \tag{26}$$

be the wavelength corresponding to the center frequency. Then, under Assumptions 2, **3**, and Lemma 1, we have the following upper bound on the restricted isometry constant δ of $\mathcal{F}$ over rank-1, PSD matrices:

$$\delta \leq \frac{2\pi}{A} \frac{2\lambda_c \sqrt{L\Delta_{\text{res}}}}{\Delta^2 \cos\phi \sqrt{\cos\phi}} + \mathcal{O}\left(\frac{K}{(N/A)^2} \lambda_c^{-3/2}\right) \tag{27}$$

where the order is a small constant and

$$\Delta_{\text{res}} = 2\pi \frac{c_0}{2B}, \quad \text{and} \quad \Delta = \frac{L}{\sqrt{K}}. \tag{28}$$

Proof: See Appendix D. ■

As provided in (22) and explained in [1], δ directly controls the convergence rate of GWF iterates. As such, bound in (27) establishes that the convergence behavior of GWF for multistatic imaging depends on system parameters such as the center frequency ω_c, the bandwidth B, the number of receivers N, the number of unknowns K, as well as the side length L of the scene.

Remark 1: Observe that N has a higher order than λ_c^{-1} in the second term in (27). Hence, our RIC upper bound estimate tends to 0 as $\omega_c \to \infty$, $N \to \infty$, consistent with our asymptotic isometry result for $\mathcal{F}$. Specifically, the first term in (27) captures the perturbation from the limit when the central frequency is finite, whereas the second term characterizes the perturbation due to having finite number of receivers. In fact, the second term directly arises from the closed form error of a Riemann sum approximation to an integration over look directions of the receivers.

Remark 2: The Riemann sum error behaves in an inverted manner to the first term with respect to the central frequency of the transmitted signal is increased, given a fixed imaging aperture and number of look directions. This is indeed an expected outcome, as the data collection manifold corresponds to a larger area of the 2D Fourier spectrum of the scene as the central frequency is increased while the imaging aperture is fixed. As a result, N number of look directions corresponds to a poorer discretization of the data collection manifold, and the factor of $\lambda_c^{-3/2}$ in the second term in (27) relates directly to this phenomenon.

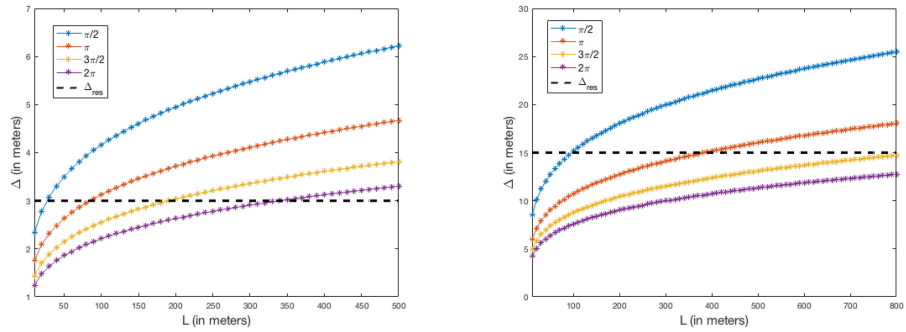

(a) Active Regime. Center frequency was set at 10 GHz and bandwidth at 50 MHz.

(b) Passive Regime. Center frequency was set at 1.9 GHz and bandwidth at 10 MHz (similar to CDMA cell phone signals).

Fig. 1. Curves of lower bound on the pixel spacing, Δ for various values of aperture lengths at active and passive regimes.

Using the decoupled nature of our upper bound estimate on the RIC, we quantify the minimal pixel spacing at which the exact recovery guarantees of GWF can hold.

Corollary 1 (Resolution Bound): Suppose we have sufficiently many receivers, i.e., $N^2 \gg K$, such that the second term in (27) is negligible. Then GWF guarantees exact recovery if

$$\Delta \geq \sqrt{\frac{2\pi}{A}\frac{2\lambda_c\sqrt{L\Delta_{\text{res}}}}{0.214\cos\phi\sqrt{\cos\phi}}}. \tag{29}$$

Proof: Assuming $N^2 \gg K$, the second term in (27) in the upper bound of δ vanishes. Recall that exact recovery is guaranteed via GWF if δ is less than or equal to 0.214. Upper bounding the RIC bound in (27), we have

$$\frac{2\pi}{A}\frac{2\lambda_c\sqrt{L\Delta_{\text{res}}}}{\Delta^2\cos\phi\sqrt{\cos\phi}} \leq 0.214. \tag{30}$$

The rest follows by rearranging (30). ■

Notably, even with $N \to \infty$, (29) is the absolute best resolution at which exact multi-static imaging is possible by GWF. Hence, Corollary 1 yields a fundamental bound for the pixel spacing in designing realizable imaging systems with finite number of receivers.

The resolution bound of Corollary 1 corresponds to the super-resolution regime when reconstructing small scenes in both active, and passive scenarios, as depicted in Fig. 1(a) and Fig. 1(b), respectively. Note that as L gets large, the lower bound eventually becomes greater than the range resolution limit of the Fourier-based methods. This is in agreement with our theoretical arguments, which are established under a small scene approximation. It should also be stressed that our lower bound abides by the sufficient condition for exact recovery, but it is not a necessary one. Therefore, while recovery of scenes at a higher resolution than Δ_{res} may still be possible via GWF, it is not covered by the theory in [1].

Additionally, the sufficient number of receivers for (29) to hold is $N^2 \geq \mathcal{O}(K)$. Since $M = \mathcal{O}(L)$ by (25), this implies that super-resolution imaging via GWF requires a sample complexity of at least $MN^2 = \mathcal{O}(K^{3/2})$. We reduce this complexity result by the following corollary, which quantifies the minimal sample requirement for exact multi-static imaging via GWF at a fixed pixel spacing that abides the lower bound of Corollary 1.

Corollary 2 (Sample Complexity): Given the final result of Theorem 1, exact multistatic imaging condition for GWF is satisfied at the following sample complexity:

$$MN^2 = \mathcal{O}(K^{5/4}). \tag{31}$$

Proof: Reorganizing the upper bound on δ in Theorem 1, we have

$$c_1\frac{K}{L\sqrt{L}} + c_2\frac{K}{N^2} = \tilde{\delta} \tag{32}$$

where c_1, c_2 are $\mathcal{O}(1)$ as functions of K and N. Now, for any fixed pixel spacing Δ, we have $L = \mathcal{O}(\sqrt{K})$. Thus,

$$\tilde{c}_1\, K^{1/4} + \tilde{c}_2\frac{K^{3/4}}{N^2}K^{1/4} = \tilde{\delta} \tag{33}$$

for some $\tilde{c}_1, \tilde{c}_2 = \mathcal{O}(1)$. Observe that $K^{1/4}$ factor in the first term of the left-hand side of (33) is non-vanishing and hence at best yields the RIC upper bound of $\tilde{\delta} = \mathcal{O}(K^{1/4})$. Now from Assumption 1, we have $M = \mathcal{O}(L)$. Thus, the minimal sample complexity in which the RIC upper bound is in the order of $K^{1/4}$ is achieved when $N^2 = \mathcal{O}(K^{3/4})$. Therefore,

$$(\tilde{c}_1 + \hat{c}_2)K^{1/4} = \tilde{\delta} \tag{34}$$

when $MN^2 = \mathcal{O}(K^{5/4})$. ■

In addition to the minimal sample complexity, Corollary 2 yields a rate at which the algorithm performance deteriorates. Clearly, from (34), our ability to fine sample the scene while attaining the exact recovery guarantees of GWF for multi-static imaging depends on the dimension of the problem, at a rate $K^{1/4}$, or equivalently, $\sqrt{L}$. This, again, is consistent with our theoretical arguments as we derive our results through a small scene approximation.

The fact that the upper bound of δ has a non-vanishing $K^{1/4}$ factor reveals an interesting phenomenon that is also observed in the performance of spectral initialization in phase retrieval literature, even when the measurement vectors are random. This degradation with the increasing dimension of the unknown is not captured in the probabilistic analysis with random measurement

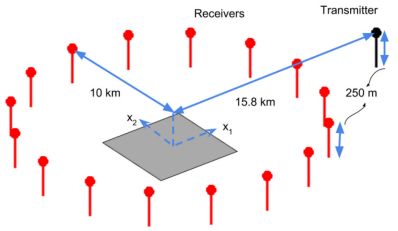

Fig. 2. Illustration of the multistatic imaging set-up for numerical simulations. (Not to scale.)

vectors, yet is indeed a significant issue which forms the basis for sample truncation in computing the initialization and gradient estimates [53].

Specifically for deterministic, wave-based multistatic imaging problems, Corollary 2 necessitates a system design such that the controllable constants in (34) sufficiently suppress the $K^{1/4}$ factor. This promotes GWF as a highly applicable method in passive imaging scenarios where the range resolution is limited, or in active imaging scenarios where small, isolated extended targets are being imaged, with possible extensions and applications in spot-light mode synthetic aperture radar [54].

IV. Numerical Simulations

In this section, we provide several numerical simulations demonstrating veracity of the theory presented in Section III. Note that the results in Section III present an upper bound to achieve the sufficient condition of exact recovery via GWF. Thereby, even if the specific guarantees we have derived are not satisfied, exact recovery could be achieved by the algorithm. The following multistatic set-up is common to all simulations presented in this section, and conforms to the assumptions laid out in Section III.

1) There is a single transmitter located at $[15.8, 0, 0.25]$ km.
2) The transmitted waveform has unit amplitude frequency spectrum.
3) Varying number of receivers are distributed equidistant on an arc of a circle of radius 10 km from the scene center at a height of 0.25 km.
4) The scene of interest is square with flat topography.

Fig. 2 illustrates the multistatic set-up used in this section. Note that the illustration is not to scale.

The figure-of-merit we use throughout is the mean square error (MSE) of the reconstructed scene. This is computed by taking the per pixel difference between the true scene and the reconstructed scene and averaging the squares of the differences.

In all experiments presented, our data is synthetically generated using our received signal model in (1) under the single-scattering assumption, i.e., the Born approximation. In Sections IV-A, IV-B, and IV-C, a single parameter is varied in each set of experiment while all other relevant parameters are fixed. The parameters are chosen in the active and passive imaging ranges. Fig. 3 shows the scene used for all experiments in the subsequent sections. Finally, in Section IV-D, we provide simulations that depict the performance of GWF in non-ideal

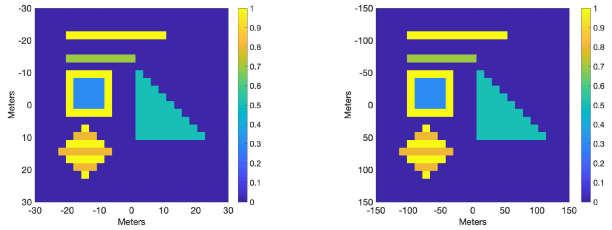

(a) Active case. (b) Passive case.

Fig. 3. The ground truth used in the numerical experiments. The colorbar refers to the reflectivity of the resolution bins. L is set as 60 m in the active, 300 m in the passive case.

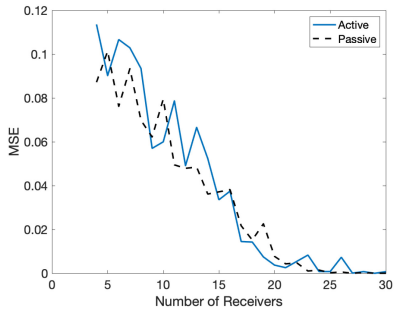

Fig. 4. Number of receivers vs. MSE of the reconstruction after 4000 iterations of GWF for active and passive radar parameters. Blue solid line is the curve for active radar parameters and black dashed line is for the passive radar parameters. Number of frequency samples was held constant at 64 and $K = 625$ for both cases. The pixel spacing was set at 2.4 m for active case and 12 m for passive. The center frequency was set at 10 GHz and 1.9 GHz for active and passive cases, respectively. The bandwidth was set at 50 MHz and 10 MHz for active and passive cases, respectively.

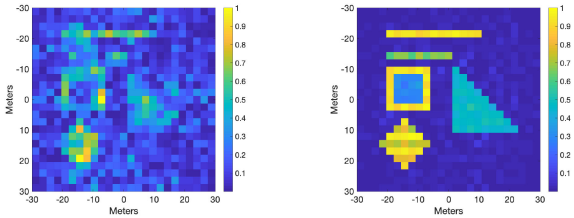

(a) 12 receivers. (b) 24 receivers.

Fig. 5. Sample reconstructions after 4000 iterations of GWF for active imaging case with varying number of receivers. Bandwidth was set at 50 MHz with center frequency of 10 GHz. Number of frequency samples was held constant at 64 and $K = 625$. The pixel spacing was set at 2.4 m.

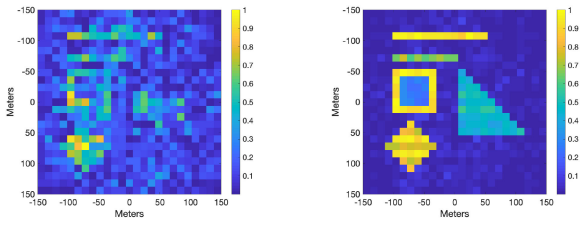

(a) 12 receivers. (b) 24 receivers.

Fig. 6. Sample reconstructions after 4000 iterations of GWF for passive imaging case with varying number of receivers. Bandwidth was set at 10 MHz with center frequency of 1.9 GHz. Number of frequency samples was held constant at 64 and $K = 625$. The pixel spacing was set at 12 m.

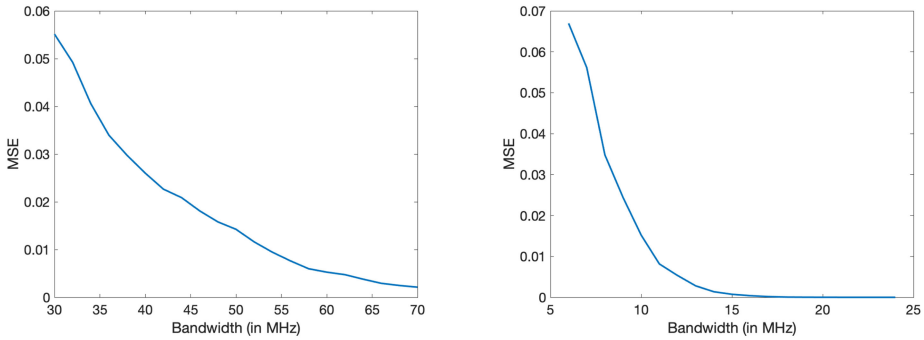

(a) Active Regime. Center frequency was set at 10 GHz and bandwidth ranged from 30 MHz to 70 MHz.

(b) Passive Regime. Center frequency was set at 1.9 GHz and bandwidth ranged from 6 MHz to 24 MHz.

Fig. 7. Bandwidth vs. MSE of the reconstruction after 4000 iterations of GWF for active and passive radar parameters. Number of frequency samples was held constant at 64 and $K = 625$ for both cases. The pixel spacing was set at 2.4 m for active case and 12 m for passive.

conditions, namely under additive noise at low signal-to-noise ratios (SNR).

A. *Effect of Number of Receivers*

The first series of numerical experiments are designed to verify the effect of the number of receivers on the performance of GWF reconstruction. In (27), the second term involves the square of the number of receivers, N^2, in the denominator. Thus, we expect the number of receivers to have significant effect on the quality of the reconstruction. To verify the effect of the number of receivers on the reconstruction, we ran a series of simulations with varying number of receivers while fixing all other relevant parameters in active or passive radar regimes.

Fig. 4 shows the MSE of the resulting reconstruction versus the number of receivers for active and passive imaging. Blue solid line is the result for the active case while black dashed line is for the passive case. For the active case, the bandwidth was held at $B = 50$ MHz with the center frequency at $\omega_c = 10$ GHz for Fourier-based range resolution of $\Delta_{\text{res}} = 3$ m. For the passive case, $B = 10$ MHz and $\omega_c = 1.9$ GHz for $\Delta_{\text{res}} = 15$ m. The pixel spacing was chosen such that it was smaller than the Fourier-based range resolution for each case. Namely, $\Delta = 2.4$ m and $\Delta = 12$ m for the active and passive cases, respectively. The number of unknowns was held constant at $K = 625$ for both cases. The GWF algorithm was performed for 4000 iterations for comparison purposes. Since the RIC directly affects the rate of convergence of GWF, we expect to see smaller MSE as the number of receivers grows. This behavior is clearly present in both the active and passive cases as can be readily observed in Fig. 4. In both cases, we observed exact convergence behavior from 10 receivers onward. However, as expected, the convergence rate is slower with smaller number of receivers.

As a visual confirmation of the experimental verification, sample reconstructions at two different number of receivers (12 and 24) is provided in Figs. 5 and 6 for active and passive regimes, respectively.

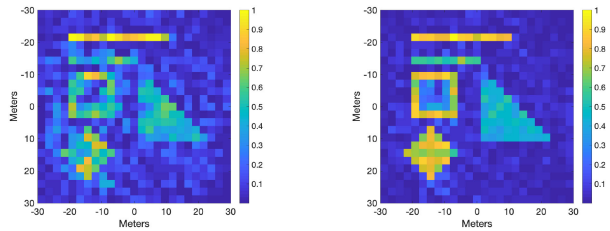

(a) 40 MHz bandwidth.

(b) 60 MHz bandwidth.

Fig. 8. Sample reconstructions after 4000 iterations of GWF for active imaging case with varying bandwidth. 18 receivers were used for reconstruction with center frequency of 10 GHz. Number of frequency samples was held constant at 64 and $K = 625$. The pixel spacing was set at 2.4 m.

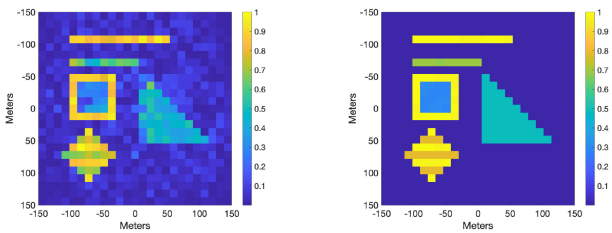

(a) 12 MHz bandwidth.

(b) 20 MHz bandwidth.

Fig. 9. Sample reconstructions after 4000 iterations of GWF for passive imaging case with varying bandwidth. 18 receivers were used for reconstruction with center frequency of 1.9 GHz. Number of frequency samples was held constant at 64 and $K = 625$. The pixel spacing was set at 12 m.

B. *Effect of Bandwidth/Range Resolution*

Next we examine the effect of the bandwidth on the convergence behavior. Both terms in (27) includes square root of Δ_{res}, the range resolution, in the numerator. This suggests that there is an inverse relationship between the bandwidth and RIC. Similar to above, we test the effect of bandwidth on the convergence behavior of GWF algorithm, and we ran a series of GWF reconstruction on the same scene while varying the bandwidth and holding other relevant parameters fixed. The number of receivers used for the experiments was fixed at $N = 18$. All

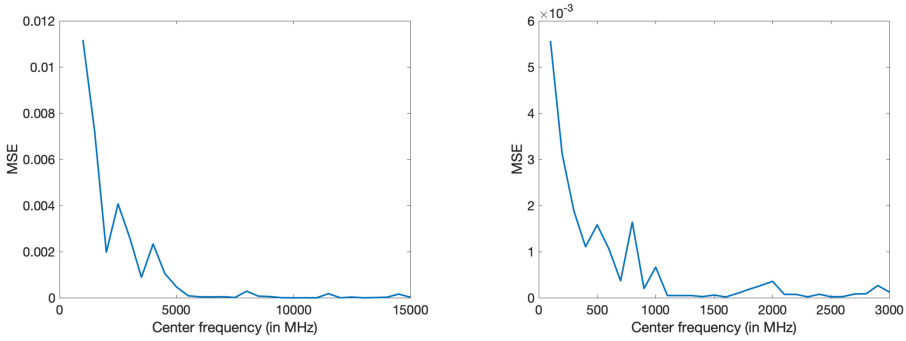

(a) Active Regime. (b) Passive Regime.

Fig. 10. Center frequency vs. MSE of the reconstruction after 4000 iterations of GWF for active and passive radar parameters. Number of frequency samples was held constant at 64 and $K = 625$ for both cases. The pixel spacing was set at 2.4 m for active case and 12 m for passive. The bandwidth was fixed at 50 MHz and 10 MHz for active and passive cases, respectively.

other parameters were held to the same values as in the previous subsection.

Fig. 7 summarizes the result of these experiments. Fig. 7(a) shows the bandwidth vs. MSE curve for active case. We varied the bandwidth in the range of 30 MHz to 70 MHz. Fig. 7(b) shows the same curve for the passive case where the bandwidth was varied between 6 MHz and 24 MHz. Examining the two figures, we clearly see that higher bandwidth results in smaller MSE, and hence faster convergence to exact solution. This agrees with the theoretical bound in (27). As before, we provide visual confirmation in form of sample reconstructions in Figs. 8 and 9 for active and passive regimes, respectively.

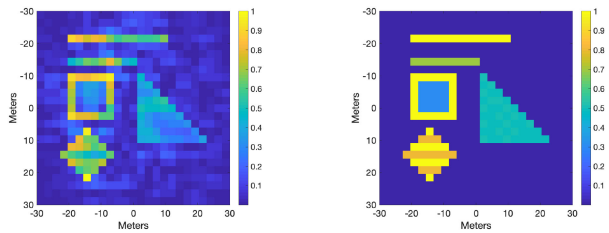

(a) 1 GHz center frequency. (b) 12 GHz center frequency.

Fig. 11. Sample reconstructions after 4000 iterations of GWF for active imaging case with varying center frequencies. 32 receivers were used for reconstruction with bandwidth fixed at 50 MHz. Number of frequency samples were set as 64 and $K = 625$. The pixel spacing was set at 2.4 m.

C. *Effect of Center Frequency*

The first term of (27) is inversely proportional to the center frequency of the transmitted waveform and as such we expect the center frequency to improve the convergence behavior of GWF as the center frequency gets larger. We examined numerically, the effect of center frequency on the exact reconstruction and the convergence rate by, again, running a series of numerical simulations where we varied the center frequency while keeping other relevant variables constant. To minimize the effect of the second term on the RIC and better evaluate the impact of central frequency in the super-resolution regime, we increased the number of receivers used in these experiments to $N = 32$ for both cases.

Figs. 10(a) and 10(b) show the results of simulated experiments for active and passive scenarios, respectively. For active case, we varied the center frequency in the range between 0.5 GHz and 15 GHz. For the passive case, the range was restricted to 0.1 GHz to 3 GHz to reflect realistic values for sources of opportunity. In both cases, we observe a behavior of downward trend in MSE as the center frequency increases, albeit, not as drastic as in other parameters. This is due to the fact that the central frequency appears inverted in the two terms of the RIC upper bound. The decaying trend of our experiments agrees with the notion that the order constant of the second term in the RIC upper bound adequately suppresses $\lambda_c^{-3/2}$, as $N^2 = \mathcal{O}(K)$ proves to be sufficient for super-resolution.

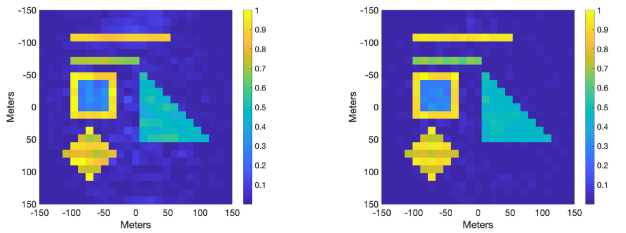

(a) 1 GHz center frequency. (b) 2 GHz center frequency.

Fig. 12. Sample reconstructions after 4000 iterations of GWF for passive imaging case with varying center frequencies. 32 receivers were used for reconstruction with bandwidth fixed at 10 MHz. Number of frequency samples were set as 64 and $K = 625$. The pixel spacing was set at 12 m.

Notice, however, that in the active case, larger center frequency value is needed to achieve similar performance as in the passive case. This is attributable to the fact that the first term is proportional to $\sqrt{L\Delta_{\text{res}}}/\Delta^2$. With the active parameters, this term is approximately 8 times that of the passive case. Thus, the center frequency needs to be higher to compensate for the difference. Figs. 11 and 12 show sample reconstructions at two different center frequencies for active and passive regimes, respectively.

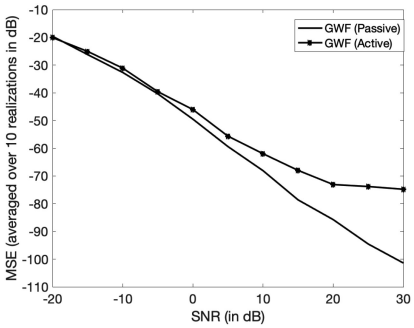

Fig. 13. Received signal SNR vs. MSE of the reconstruction after 4000 iterations of GWF. SNR values depict those in the linear measurements collected at each receiver, prior to correlations. Dotted and solid curves are for active and passive radar parameters, respectively. Number of frequency samples were fixed as 64, with $K = 625$ for both cases. The pixel spacing was set at 2.4 m for active case and 12m for passive. The center frequency was set at 10 GHz and 1.9 GHz for active and passive cases, respectively. The bandwidth was set at 50 MHz and 10 MHz for active and passive cases, respectively.

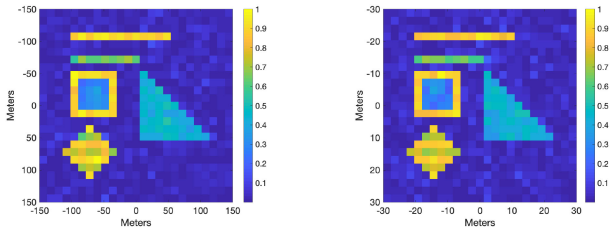

(a) 0 dB SNR (passive). (b) 0 dB SNR (active).

Fig. 14. Sample reconstructions after 4000 iterations of GWF with 0 dB SNR at the receivers. 30 receivers were used for reconstruction. Number of frequency samples was held constant at 64 and $K = 625$. The pixel spacing was set at 12 m, and 2.4 m, respectively.

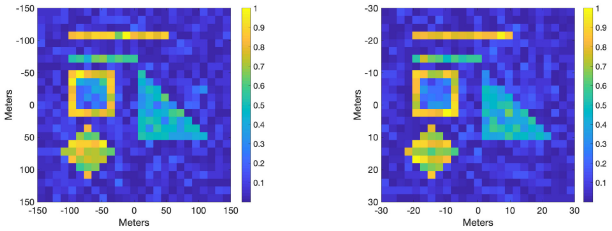

(a) -5 dB SNR (passive). (b) -5 dB SNR (active).

Fig. 15. Sample reconstructions after 4000 iterations of GWF with -5 dB SNR at the receivers. 30 receivers were used for reconstruction. Number of frequency samples was held constant at 64 and $K = 625$. The pixel spacing was set at 12 m, and 2.4 m, respectively.

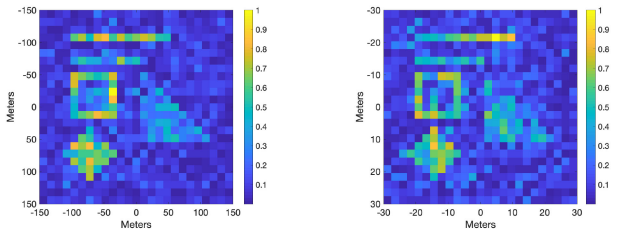

(a) -10 dB SNR (passive). (b) -10 dB SNR (active).

Fig. 16. Sample reconstructions after 4000 iterations of GWF with -10 dB SNR at the receivers. 30 receivers were used for reconstruction. Number of frequency samples was held constant at 64 and $K = 625$. The pixel spacing was set at 12 m, and 2.4 m, respectively.

D. *Effect of Additive Noise*

Next, we evaluate the robustness of the proposed method for interferometric multi-static radar imaging, in passive, and active cases. As before, we use a flat spectrum signal with 10 MHz bandwidth centered around 1.9 GHz frequency in the passive, and a 50 MHz bandwidth centered around 10 GHz frequency in the active experiments. We incorporate additive, zero-mean white Gaussian noise on the linear signal model at the receivers, and consider SNR levels varying from -20 to 30 dB. Fig. 13 demonstrates the reconstruction MSE with respect to the received signal SNR with 5 dB increments, with errors averaged over 10 realizations. The MSE curves indicate that GWF is robust to additive noise at the receivers in both active and passive cases, and the performance of the algorithm degrades predictably with decreasing SNRs, with steady decay in MSE as the SNR at the receivers improve.

It should be noted that the correlation operation amplifies the noise variance, hence the interferometric measurements processed in the experiments have lower SNR than the specified levels at the receivers. Nonetheless, we observe that the reconstruction performance of GWF degrades gracefully as SNR decrases, as Figs. 14, 15 and 16 demonstrate that GWF is capable of producing highly accurate imagery with 0 dB in the received signals at the antennas. However with SNRs below -10 dB the algorithm performance degrades noticeably, which motivates filtering or sample truncation at the implementation of GWF in low SNR scenarios.

V. Conclusion

In this paper, we utilize GWF theory developed in [1] for exact multistatic imaging of extended targets by designing the underlying imaging parameters such that the sufficient condition for exact recovery is satisfied. Our work has two significant contributions. 1) Unlike the state-of-the-art interferometric inversion methods based on LRMR, GWF avoids lifting the problem. As a result, it is computationally efficient and does not require large memory allocations, making it suitable for practical applications. 2) We demonstrate that the underlying imaging parameters can be designed so that the RIP over rank-1, PSD matrices is satisfied by a *deterministic* lifted forward model.

We first show the asymptotic isometry of the lifted forward model, $\mathcal{F}$, of interferometric multistatic radar, as the center frequency and the number of receivers go to infinity. We then proceed with estimating the deviation from the asymptotic behavior when imaging parameters are finite, and derive an upper bound for the RIC of $\mathcal{F}$ over the set of rank-1, PSD matrices. Hence, we identify the relation of imaging parameters to the sufficient condition of exact recovery. Using the RIC upper bound, we determine a lower limit for pixel spacing to achieve exact recovery. This limit is superior to the Fourier-based range resolution for sufficiently small scenes. Furthermore, we determine the

minimal sample complexity needed for RIC upper bound to be sufficiently small, hence identify the practical requirements for reconstruction when designing a multistatic imaging system. In our numerical simulations, we evaluate the impact of the imaging parameters in our upper bound estimate of RIC in reconstruction performance, verify our theoretical results, and finally assess the performance of GWF to additive noise at low SNRs.

For future work, we will study the robustness of our method with respect to deviations from our imaging setup, such as non-equi-distant locations, or non-circular configurations of receivers. In addition, we will investigate extensions of our theory to the case involving additive noise and outliers, moving target imaging, as well as implementation of our method using real scattering data.

APPENDIX

A. Proof of Lemma 1

We first examine the 2-norm of the data. For a rank-1 $\tilde{\boldsymbol{\rho}}$, we have that $\|\tilde{\boldsymbol{\rho}}\|_F^2 = \|\boldsymbol{\rho}\|_2^4$. We can also rewrite

$$\|\mathcal{F}\tilde{\boldsymbol{\rho}}\|_2^2 = \frac{1}{M\binom{N}{2}} \sum_{i=1}^{N}\sum_{i<j}^{N}\sum_{m=1}^{M} |\langle \mathbf{L}_i^m, \boldsymbol{\rho}\rangle|^2 \left|\langle \mathbf{L}_j^m, \boldsymbol{\rho}\rangle\right|^2. \quad (35)$$

Thus, from (11), (8), and (9) we have

$$|\langle \mathbf{L}_i^m, \boldsymbol{\rho}\rangle|^2 = \sum_{k,k'} \mathrm{e}^{-\mathrm{i}\omega_m/c_0(\langle \hat{\mathbf{a}}_i^r, \mathbf{x}_k - \mathbf{x}_{k'}\rangle + \langle \hat{\mathbf{a}}^t, \mathbf{x}_k - \mathbf{x}_{k'}\rangle)} \times \rho(\boldsymbol{x}_k)\rho^*(\boldsymbol{x}_{k'}) \frac{|C_i|^2}{|\mathbf{a}_i^r|^2 |\mathbf{a}^t|^2}. \quad (36)$$

Similarly, we have that

$$|\langle \mathbf{L}_i^m, \boldsymbol{\rho}\rangle|^2 \left|\langle \mathbf{L}_j^m, \boldsymbol{\rho}\rangle\right|^2 = \sum_{k,k,'l,l'} \mathrm{e}^{-\mathrm{i}\omega_m/c_0 \Phi_{i,j}^{k,k',l,l'}} \times \rho(\boldsymbol{x}_k)\rho^*(\boldsymbol{x}_{k'})\rho(\boldsymbol{x}_{l'})\rho^*(\boldsymbol{x}_l) \frac{|C_i|^2 |C_j|^2}{|\mathbf{a}_i^r|^2 \left|\mathbf{a}_j^r\right|^2 |\mathbf{a}^t|^4} \quad (37)$$

where $\Phi_{i,j}^{k,k',l,l'}$ is as in (15). Then, under Assumption 1, we have that

$$\begin{aligned}\frac{1}{M}\sum_{m=1}^{M} \mathrm{e}^{-\mathrm{i}\frac{\omega_m}{c_0}\Phi_{i,j}^{k,k',l,l'}} &= \frac{\mathrm{e}^{-\mathrm{i}\frac{\omega_c}{c_0}\Phi_{i,j}^{k,k',l,l'}}}{M} \sum_{m=1}^{M} \mathrm{e}^{\mathrm{i}\frac{B}{2c_0}\Phi_{i,j}^{k,k',l,l'}} \times \mathrm{e}^{-\mathrm{i}\frac{(m-1)B}{Mc_0}\Phi_{i,j}^{k,k',l,l'}} \\ &= \frac{\mathrm{e}^{-\mathrm{i}\frac{\omega_c'}{c_0}\Phi_{i,j}^{k,k',l,l'}}}{M} \frac{\sin\left(\frac{B}{2c_0}\Phi_{i,j}^{k,k',l,l'}\right)}{\sin\left(\frac{B}{2Mc_0}\Phi_{i,j}^{k,k',l,l'}\right)} \\ &\approx \mathrm{e}^{-\mathrm{i}\frac{\omega_c'}{c_0}\Phi_{i,j}^{k,k',l,l'}} \operatorname{sinc}\left(\frac{B}{2c_0}\Phi_{i,j}^{k,k',l,l'}\right) \end{aligned} \quad (38)$$

where $\omega_c' = \omega_c - \frac{B}{2,M}$. The second line is from geometric sum and the last line is from small angle approximation.

Using (38) and changing the order of sum, and denoting $|\alpha_{i,j}|^2 = \frac{|C_i|^2|C_j|^2}{|\mathbf{a}_i^r|^2|\mathbf{a}_j^r|^2|\mathbf{a}^t|^4}$, we have

$$\|\mathcal{F}\tilde{\boldsymbol{\rho}}\|_2^2 = \frac{1}{\binom{N}{2}} \sum_{i<j} |\alpha_{i,j}|^2 \sum_{k,k',l,l'} \mathrm{e}^{-\mathrm{i}\omega_c'/c_0\Phi_{i,j}^{k,k',l,l'}} \times \operatorname{sinc}\left(\frac{B}{2c_0}\Phi_{i,j}^{k,k',l,l'}\right) \tilde{\rho}(\boldsymbol{x}_k, \boldsymbol{x}_{k'})\tilde{\rho}(\boldsymbol{x}_{l'}, \boldsymbol{x}_l). \quad (39)$$

We can split (39) into two parts as

$$\begin{aligned}\|\mathcal{F}\tilde{\boldsymbol{\rho}}\|_2^2 &= \sum_{i<j} \frac{|\alpha_{i,j}|^2}{\binom{N}{2}} \left(\|\boldsymbol{\rho}\|_2^4 + \sum_{k\neq k', l\neq l'} \mathrm{e}^{-\mathrm{i}\frac{\omega_c'}{c_0}\Phi_{i,j}^{k,k',l,l'}} \times \operatorname{sinc}\left(\frac{B}{2c_0}\Phi_{i,j}^{k,k',l,l'}\right) \tilde{\rho}(\boldsymbol{x}_k, \boldsymbol{x}_{k'})\tilde{\rho}(\boldsymbol{x}_{l'}, \boldsymbol{x}_l) \right) \\ &= \sum_{i<j} \frac{|\alpha_{i,j}|^2}{\binom{N}{2}} \left(\|\tilde{\boldsymbol{\rho}}\|_F^2 + \mathrm{Re}\left\{ \sum_{k\neq k', l\neq l'} \mathrm{e}^{-\mathrm{i}\frac{\omega_c'}{c_0}\Phi_{i,j}^{k,k',l,l'}} \times \operatorname{sinc}\left(\frac{B}{2c_0}\Phi_{i,j}^{k,k',l,l'}\right) \tilde{\rho}(\boldsymbol{x}_k, \boldsymbol{x}_{k'})\tilde{\rho}(\boldsymbol{x}_{l'}, \boldsymbol{x}_l) \right\} \right) \\ &= \sum_{i<j} \frac{|\alpha_{i,j}|^2}{\binom{N}{2}} \left(\|\tilde{\boldsymbol{\rho}}\|_F^2 + \sum_{k\neq k', l\neq l'} \mathrm{Re}\left\{ \mathrm{e}^{-\mathrm{i}\frac{\omega_c'}{c_0}\Phi_{\mathrm{i,j}}^{k,k',1,l'}} \times \operatorname{sinc}\left(\frac{B}{2c_0}\Phi_{i,j}^{k,k',l,l'}\right) \tilde{\rho}(\boldsymbol{x}_k, \boldsymbol{x}_{k'})\tilde{\rho}(\boldsymbol{x}_{l'}, \boldsymbol{x}_l) \right\} \right). \end{aligned} \quad (40)$$

Having a real-valued $\tilde{\boldsymbol{\rho}}$, we rewrite the latter term in (40) as

$$\begin{aligned} W_{i,j} &= \sum_{k\neq k', l\neq l'} \mathrm{Re}\left\{ \mathrm{e}^{-\mathrm{i}\frac{\omega_c'}{c_0}\Phi_{i,j}^{k,k',l,l'}} \operatorname{sinc}\left(\frac{B}{2c_0}\Phi_{i,j}^{k,k',l,l'}\right) \times \tilde{\rho}(\boldsymbol{x}_k, \boldsymbol{x}_{k'})\tilde{\rho}(\boldsymbol{x}_{l'}, \boldsymbol{x}_l) \right\} \\ &= \sum_{k\neq k', l\neq l'} \cos\omega_c'/c_0\Phi_{i,j}^{k,k',l,l'} \operatorname{sinc}\left(\frac{B}{2c_0}\Phi_{i,j}^{k,k',l,l'}\right) \times \tilde{\rho}(\boldsymbol{x}_k, \boldsymbol{x}_{k'})\tilde{\rho}(\boldsymbol{x}_{l'}, \boldsymbol{x}_l) \\ &= \sum_{k\neq k', l\neq l'} \mathcal{K}(\Phi_{i,j}^{k,k',l,l'})\tilde{\rho}(\boldsymbol{x}_k, \boldsymbol{x}_{k'})\tilde{\rho}(\boldsymbol{x}_{l'}, \boldsymbol{x}_l). \end{aligned} \quad (41)$$

We can further rewrite $\mathcal{K}(\Phi_{i,j}^{k,k',l,l'})$ (41) using trigonometric identity as

$$\mathcal{K}(\Phi_{i,j}^{k,k',l,l'}) = \frac{\sin\left[\frac{\left(\omega_c' + \frac{B}{2}\right)\Phi_{i,j}^{k,k',l,l'}}{c_0}\right] - \sin\left[\frac{\left(\omega_c' - \frac{B}{2}\right)\Phi_{i,j}^{k,k',l,l'}}{c_0}\right]}{B\frac{\Phi_{i,j}^{k,k',l,l'}}{c_0}} \quad (42)$$

which proves the claim.

B. Proof of Proposition 1

First we express $\mathcal{K}$ as

$$\mathcal{K}(\Phi_{i,j}^{k,k',l,l'}) = \frac{\sin\left[\frac{\left(\omega_c'+\frac{B}{2}\right)\Phi_{i,j}^{k,k',l,l'}}{c_0}\right] - \sin\left[\frac{\left(\omega_c'-\frac{B}{2}\right)\Phi_{i,j}^{k,k',l,l'}}{c_0}\right]}{B\frac{\Phi_{i,j}^{k,k',l,l'}}{c_0}}$$
$$= \frac{\omega_c'}{B}\left\{s_1(\Phi_{i,j}^{k,k',l,l'}) - s_2(\Phi_{i,j}^{k,k',l,l'})\right\} + \frac{1}{2}\left\{s_1(\Phi_{i,j}^{k,k',l,l'}) + s_2(\Phi_{i,j}^{k,k',l,l'})\right\} \quad (43)$$

where

$$s_1(\Phi_{i,j}^{k,k',l,l'}) = \operatorname{sinc}\left[\frac{\left(\omega_c'+\frac{B}{2}\right)\Phi_{i,j}^{k,k',l,l'}}{c_0}\right]$$
$$s_2(\Phi_{i,j}^{k,k',l,l'}) = \operatorname{sinc}\left[\frac{\left(\omega_c'-\frac{B}{2}\right)\Phi_{i,j}^{k,k',l,l'}}{c_0}\right] \quad (44)$$

Given (43), it suffices to prove that

$$\lim_{\omega_c'\to\infty}\frac{\omega_c'}{B}\operatorname{sinc}\left[\left(\omega_c'+\frac{B}{2}\right)\frac{\Phi_{i,j}^{k,k',l,l'}}{c_0}\right] = \frac{c_0\pi}{B}\delta(\Phi_{i,j}^{k,k',l,l'}) \quad (45)$$

$$\lim_{\omega_c'\to\infty}\frac{\omega_c'}{B}\operatorname{sinc}\left[\left(\omega_c'-\frac{B}{2}\right)\frac{\Phi_{i,j}^{k,k',l,l'}}{c_0}\right] = \frac{c_0\pi}{B}\delta(\Phi_{i,j}^{k,k',l,l'}). \quad (46)$$

This can be proved using similar machinery to proving the delta function limit for sequence of scaled sinc functions. We prove the first equation (45). The second equation follows similarly.

Let $f \in S(\mathbb{R})$ be a smooth test function, where $S(\mathbb{R})$ is the Schwartz space. Then we need to prove that

$$\lim_{\omega_c'\to\infty}\int_{-\infty}^{\infty} g_{\omega_c'}(x)f(x)dx = \frac{c_0\pi}{B}f(0). \quad (47)$$

where

$$g_{\omega_c'}(x) = \frac{\omega_c'}{B}\operatorname{sinc}\left[\left(\omega_c'+\frac{B}{2}\right)\frac{x}{c_0}\right] \quad (48)$$

Let $\epsilon > 0$ and break-up the integral into two parts.

$$\int_{-\infty}^{\infty} K(x)f(x)dx = \int_{|x|\geq\epsilon} g_{\omega_c'}(x)f(x)dx + \int_{|x|\leq\epsilon} g_{\omega_c'}(x)f(x)dx. \quad (49)$$

The first part of the integral is

$$\int_{|x|\geq\epsilon} g_{\omega_c'}(x)f(x)dx = \int_{\epsilon}^{\infty} g_{\omega_c'}(x)f(x)dx + \int_{-\infty}^{-\epsilon} g_{\omega_c'}(x)f(x)dx \quad (50)$$

We compute the first part of (50). Integrating by parts,

$$\int_{\epsilon}^{\infty} g_{\omega_c'}(x)f(x)dx = \frac{\frac{c_0}{B}\omega_c'}{\omega_c'+\frac{B}{2}}\left[-\frac{f(x)\cos\left(\frac{\left(\omega_c'+\frac{B}{2}\right)x}{c_0}\right)}{x\left(\omega_c'+\frac{B}{2}\right)}\Big|_{\epsilon}^{\infty} + \int_{\epsilon}^{\infty}\frac{xf'(x)-f(x)}{x^2}\frac{\cos\left(\left(\omega_c'+\frac{B}{2}\right)\frac{x}{c_0}\right)}{\left(\omega_c'+\frac{B}{2}\right)}\right] \quad (51)$$

Since $f \in S(\mathbb{R})$, taking the limit as $\omega_c' \to \infty$, (51) goes to 0. Similarly, we can see that the second integral in (50) also goes to zero. Thus,

$$\lim_{\omega_c'\to\infty}\int_{|x|\geq\epsilon} g_{\omega_c'}(x)f(x)dx = 0 \quad (52)$$

Now, the second integral in (49) can be rewritten as

$$\int_{-\epsilon}^{\epsilon} g_{\omega_c'}(x)(f(x)-f(0))dx + f(0)\int_{-\epsilon}^{\epsilon} g_{\omega_c'}(x)dx \quad (53)$$

The first integral can be rewritten as

$$\frac{c_0}{B}\frac{\omega_c'}{\omega_c'+\frac{B}{2}}\int_{-\epsilon}^{\epsilon}\sin\left(\left(\omega_c'+\frac{B}{2}\right)\frac{x}{c_0}\right)\frac{f(x)-f(0)}{x}dx \quad (54)$$

Since $f \in S(\mathbb{R})$, we can use *Riemann-Lebesgue lemma* to conclude that (54) goes to zero as $\omega_c' \to \infty$ [55].

For second integral, we have

$$\frac{c_0}{B}\frac{\omega_c'}{\omega_c'+\frac{B}{2}}f(0)\int_{-\epsilon}^{\epsilon}\frac{\sin\left(\left(\omega_c'+\frac{B}{2}\right)\frac{x}{c_0}\right)}{x}dx. \quad (55)$$

After change of variables $u = (\omega_c'+\frac{B}{2})\frac{x}{c_0}$, we have

$$\frac{c_0}{B}\frac{\omega_c'}{\omega_c'+\frac{B}{2}}f(0)\int_{-\epsilon\left(\omega_c'+\frac{B}{2}\right)/c_0}^{\epsilon\left(\omega_c'+\frac{B}{2}\right)/c_0}\frac{\sin u}{u}du \to \frac{c_0\pi}{B}f(0) \quad (56)$$

as $\omega_c' \to \infty$. We can use similar argument for where

$$g_{\omega_c'}(x) = \frac{\omega_c'}{B}\operatorname{sinc}\left[\left(\omega_c'-\frac{B}{2}\right)\frac{x}{c_0}\right] \quad (57)$$

C. Proof of Proposition 2

Without loss of generality, let the receivers and transmitters have common elevation angle ϕ such that

$$\hat{\mathbf{a}}_i^r = [\cos\phi\cos\theta_i, \cos\phi\sin\theta_i, \sin\phi]^T \quad (58)$$

$$\hat{\mathbf{a}}^t = [\cos\phi\cos\theta_t, \cos\phi\sin\theta_t, \sin\phi]^T. \quad (59)$$

where θ_i is the azimuth angle of the i-th receivers look-direction, θ_t is the azimuth angle of the transmitter look-direction and ϕ is the elevation angle. Furthermore, we have that for any k and k'

$$\boldsymbol{x}_k - \boldsymbol{x}_{k'} = \|\boldsymbol{x}_k - \boldsymbol{x}_{k'}\|\,[\cos\theta_{k,k'}, \sin\theta_{k,k'}]^T \quad (60)$$

where $\theta_{k,k'}$ is the angle of the vector $\boldsymbol{x}_k - \boldsymbol{x}_{k'}$. Then we have that

$$\frac{\Phi_{i,j}^{k,k',l,l'}}{\cos\phi} = \|\boldsymbol{x}_k - \boldsymbol{x}_{k'}\|\left(\cos(\theta_i - \theta_{k,k'}) + \cos(\theta_t - \theta_{k,k'})\right) - \|\boldsymbol{x}_l - \boldsymbol{x}_{l'}\|\left(\cos(\theta_j - \theta_{l,l'}) + \cos(\theta_t - \theta_{l,l'})\right). \quad (61)$$

Thus, for the non-diagonal terms where $k \neq k'$, $l \neq l'$ we have that $\Phi_{i,j}^{k,k',l,l'} = 0$ if

$$\frac{\|\boldsymbol{x}_k - \boldsymbol{x}_{k'}\|}{\|\boldsymbol{x}_l - \boldsymbol{x}_{l'}\|}(\cos(\theta_i - \theta_{k,k'}) + \cos(\theta_t - \theta_{k,k'})) - \cos(\theta_t - \theta_{l,l'}) = \cos(\theta_j - \theta_{l,l'}). \tag{62}$$

For fixed k, k', l, l' and i, there are at most 2 values of θ_j's for which (62) is satisfied. Furthermore, we know that $|\alpha_{i,j}|^2$'s must be bounded. Thus, by Proposition 1, for each fixed k, k', l, l' where $k \neq k'$ and $l \neq l'$ we have that

$$\frac{1}{\binom{N}{2}} \sum_{i<j} |\alpha_{i,j}|^2 \lim_{\omega_c' \to \infty} \mathcal{K}(\Phi_{i,j}^{k,k',l,l'}) = \mathcal{O}\left(\frac{1}{N}\right). \tag{63}$$

Now taking the limit as $N \to \infty$, we have the desired result.

D. Proof of Theorem 1

We want to upper bound the following

$$\left| \frac{\sum_{i,i<j} |\alpha_{i,j}|^2 W_{i,j}}{\binom{N}{2}} \right| \approx \left| \frac{\alpha}{\binom{N}{2}} \sum_{i,i<j} \sum_{k,k\neq k',l,l\neq l'} \mathcal{K}(\Phi_{i,j}^{k,k',l,l'}) \times \tilde{\rho}(\boldsymbol{x}_k, \boldsymbol{x}_{k'}) \tilde{\rho}(\boldsymbol{x}_{l'}, \boldsymbol{x}_l) \right|. \tag{64}$$

where, $|\alpha_{i,j}|^2 \approx \alpha = \frac{|C|^4}{(\boldsymbol{a}_1^r)^4 (\boldsymbol{a}^t)^2}$ by Assumption 3. Without loss of generality we set $\alpha = 1$. We begin by noting that

$$\Phi_{i,j}^{k,k',l,l'} = (\hat{\mathbf{a}}_i + \hat{\mathbf{a}}_t) \cdot (\boldsymbol{x}_k - \boldsymbol{x}_{k'}) + \beta_j^{l,l'}. \tag{65}$$

where $\beta_j^{l,l'} = -(\hat{\mathbf{a}}_j + \hat{\mathbf{a}}_t) \cdot (\boldsymbol{x}_l - \boldsymbol{x}_{l'})$. Thus, fixing l, l', and k, we have convolution between $\mathcal{G}$ and ρ. Let

$$\mathcal{G}_{i,j}(\boldsymbol{x}_k - \boldsymbol{x}_{k'}) = \mathcal{K}((\hat{\mathbf{a}}_i + \hat{\mathbf{a}}_t) \cdot (\boldsymbol{x}_k - \boldsymbol{x}_{k'}) + \beta_j^{l,l'}). \tag{66}$$

We take the Fourier Transform of $\mathcal{G}_{i,j}$ and ρ to represent the convolution. Denoting, $\hat{\mathcal{G}}_{i,j}$ as the Fourier Transform of $\mathcal{G}_{i,j}$, we have

$$\sum_{k\neq k'} \sum_{l\neq l'} \mathcal{K}(\Phi_{i,j}^{k,k',l,l'}) \tilde{\rho}(\boldsymbol{x}_k, \boldsymbol{x}_{k'}) \tilde{\rho}(\boldsymbol{x}_{l'}, \boldsymbol{x}_l) = \frac{1}{4\pi^2} \sum_{l\neq l'} \tilde{\rho}(\boldsymbol{x}_l, \boldsymbol{x}_{l'}) \sum_k \rho(\boldsymbol{x}_k) \int \mathrm{e}^{\mathrm{i}\boldsymbol{\omega}\cdot\boldsymbol{x}_k} \hat{\mathcal{G}}_{i,j}(\boldsymbol{\omega}) \hat{\rho}(\boldsymbol{\omega}) d\boldsymbol{\omega} \tag{67}$$

To compute $\hat{\mathcal{G}}_{i,j}$, we first rewrite $\mathcal{G}_{i,j}$ as

$$\mathcal{G}_{i,j}(\boldsymbol{x}_k) = \frac{\omega_c' + \frac{B}{2}}{B} \operatorname{sinc}\left(\frac{\omega_c' + \frac{B}{2}}{c_0}((\hat{\mathbf{a}}_i + \hat{\mathbf{a}}_t) \cdot \boldsymbol{x}_k + \beta_j^{l,l'})\right) - \frac{\omega_c' - \frac{B}{2}}{B} \operatorname{sinc}\left(\frac{\omega_c' - \frac{B}{2}}{c_0}((\hat{\mathbf{a}}_i + \hat{\mathbf{a}}_t) \cdot \boldsymbol{x}_k + \beta_j^{l,l'})\right). \tag{68}$$

Let $\boldsymbol{x}_k = [x_1^k, x_2^k]^T$, $\boldsymbol{\omega} = [\omega_1, \omega_2]^T$ and θ_i be the azimuth angle of the i-th receiver's look-direction. Then, given (68), the Fourier Transform of $\mathcal{G}$ and using the assumption that $\hat{\boldsymbol{a}}_t = [1, 0]^T$,

$$\hat{\mathcal{G}}_{i,j}(\boldsymbol{\omega}) = \frac{c_0}{B} \frac{K}{L} \mathrm{e}^{\mathrm{i}\omega_1 \gamma_{i,j}^{l,l'}} S(\boldsymbol{\omega}) R(\omega_1) \tag{69}$$

where

$$\gamma_{i,j}^{l,l'} = \frac{\beta_j^{l,l'}}{\cos\phi(\cos\theta_i + 1)} \tag{70}$$

$$R(\omega_1) = \frac{1}{\cos\phi(\cos\theta_i + 1)} \left[\operatorname{rect}\left(\frac{\omega_1}{2\frac{(\omega_c' + \frac{B}{2})\cos\phi(\cos\theta_i + 1)}{c_0}} \right) - \operatorname{rect}\left(\frac{\omega_1}{2\frac{(\omega_c' - \frac{B}{2})\cos\phi(\cos\theta_i + 1)}{c_0}} \right) \right] \tag{71}$$

and

$$S(\boldsymbol{\omega}) = \operatorname{sinc}\left(\left(\omega_2 - \omega_1 \frac{\sin\theta_i}{\cos\theta_i + 1} \right) \frac{L}{2} \right). \tag{72}$$

Noting that R is only non-zero where $\frac{(\omega_c' - B/2)}{c_0} \cos\phi(\cos\theta_i + 1) \leq \omega_1 \leq \frac{(\omega_c' + B/2)}{c_0} \cos\phi(\cos\theta_i + 1)$, and $\omega_c' \gg B/2$, we approximate (70) as

$$\omega_1 \gamma_{i,j}^{l,l'} \approx \frac{\omega_1 [\cos\theta_j, \sin\theta_j]^T \cdot \boldsymbol{x}_l - \boldsymbol{x}_{l'}}{\cos\theta_i + 1} + \frac{\omega_c'(x_1^l - x_1^{l'})\cos\phi}{c_0}. \tag{73}$$

Next, we note that

$$\sum_k \rho(\boldsymbol{x}_k) \mathrm{e}^{\mathrm{i}\boldsymbol{\omega}\cdot\boldsymbol{x}_k} = \hat{\rho}^*(\boldsymbol{\omega}). \tag{74}$$

Thus, interchanging the sum and the integral in (67), and plugging in (69) we have

$$\begin{aligned} &\sum_{k\neq k'} \sum_{l\neq l'} \mathcal{K}(\Phi_{i,j}^{k,k',l,l'}) \tilde{\rho}(\boldsymbol{x}_k, \boldsymbol{x}_{k'}) \tilde{\rho}(\boldsymbol{x}_{l'}, \boldsymbol{x}_l) \\ &\quad = \frac{1}{4\pi^2} \frac{c_0}{B} \frac{K}{L} \int S(\boldsymbol{\omega}) R(\omega_1) |\hat{\rho}(\boldsymbol{\omega})|^2 \times \sum_{l\neq l'} \mathrm{e}^{\mathrm{i}\omega_1 \gamma_{i,j}^{l,l'}} \tilde{\rho}(\boldsymbol{x}_l, \boldsymbol{x}_{l'}) d\boldsymbol{\omega} \qquad (75) \\ &\quad = \frac{1}{4\pi^2} \frac{c_0}{B} \frac{K}{L} \int S(\boldsymbol{\omega}) R(\omega_1) |\hat{\rho}(\boldsymbol{\omega})|^2 \times |\hat{\rho}(\boldsymbol{\omega}')|^2 d\boldsymbol{\omega} \qquad (76) \end{aligned}$$

where

$$\boldsymbol{\omega}' = \omega_1' [\cos\theta_j, \sin\theta_j]^T + \frac{\omega_c'}{c_0} \cos\phi [1, 0]^T \tag{77}$$

$$\omega_1' = \frac{\omega_1}{\cos\theta_i + 1} \tag{78}$$

Now, by employing Cauchy-Schwartz, we have

$$\begin{aligned} &\left| \int S(\boldsymbol{\omega}) R(\omega_1) |\hat{\rho}(\boldsymbol{\omega})|^2 |\hat{\rho}(\boldsymbol{\omega}')|^2 d\boldsymbol{\omega} \right| \\ &\quad \leq \sqrt{\int S^2(\omega_1', \omega_2) \tilde{R}^2(\omega_1') |\hat{\rho}(\boldsymbol{\omega}')|^4 d\omega_2 d\omega_1'} \\ &\qquad \times \sqrt{\int |\hat{\rho}(\boldsymbol{\omega})|^4 d\boldsymbol{\omega}} \end{aligned} \tag{79}$$

where

$$\tilde{R}(\omega_1') = (\cos\theta_i + 1) R((\cos\theta_i + 1)\omega_1'). \tag{80}$$

By Jensen's inequality, (79) becomes

$$\left|\int S(\boldsymbol{\omega})R(\omega_1)\left|\hat{\rho}(\boldsymbol{\omega})\right|^2\left|\hat{\rho}(\boldsymbol{\omega}')\right|^2 d\boldsymbol{\omega}\right| \leq \sqrt{\int S^2(\omega_1',\omega_2)\tilde{R}^2(\omega_1')\left|\hat{\rho}(\boldsymbol{\omega}')\right|^4 d\omega_2 d\omega_1'}\int\left|\hat{\rho}(\boldsymbol{\omega})\right|^2 d\boldsymbol{\omega} \tag{81}$$

$$= 4\pi^2\left\|\boldsymbol{\rho}\right\|_2^2\sqrt{\int S^2(\omega_1',\omega_2)\tilde{R}^2(\omega_1')\left|\hat{\rho}(\boldsymbol{\omega}')\right|^4 d\omega_2 d\omega_1'} \tag{82}$$

Noting that for any fixed ω_1,

$$\int S^2(\boldsymbol{\omega})d\omega_2 = \frac{2\pi}{L}, \tag{83}$$

we have

$$\int S^2(\omega_1',\omega_2)\tilde{R}^2(\omega_1')\left|\hat{\rho}(\boldsymbol{\omega}')\right|^4 d\omega_2 d\omega_1' = \frac{2\pi}{L}\int\tilde{R}^2(\omega_1')\left|\hat{\rho}(\boldsymbol{\omega}')\right|^4 d\omega_1'. \tag{84}$$

We use Jensen's inequality once more to get

$$\sqrt{\int S^2(\omega_1',\omega_2)\tilde{R}^2(\omega_1')\left|\hat{\rho}(\boldsymbol{\omega}')\right|^4 d\omega_2 d\omega_1'} \leq \sqrt{\frac{2\pi}{L}}\int\tilde{R}(\omega_1')\left|\hat{\rho}(\boldsymbol{\omega}')\right|^2 d\omega_1'. \tag{85}$$

Next, approximating the sum over θ_j as an integral, we have

$$\frac{1}{2\binom{N}{2}}\sum_i\frac{N}{A}\sum_{i\neq j}\int\frac{A}{N}\tilde{R}(\omega_1')\left|\hat{\rho}(\boldsymbol{\omega}')\right|^2 d\omega_1' \approx \frac{1}{A}\left(\int\tilde{R}(\omega_1')\left|\hat{\rho}(\boldsymbol{\omega}')\right|^2 d\omega_1' d\theta_j + E_R\right), \tag{86}$$

where E_R denotes the Riemann sum error, A is the aperture of look directions in the imaging setup.

We first consider the inner integration over ω_1', where $\boldsymbol{\omega}' = [\omega_1', \theta_j]$. Using Cauchy-Schwartz and Jensen's inequalities,

$$\int_A\left[\int\frac{1}{|\omega_1'|}\tilde{R}(\omega_1')\left|\omega_1'\right|\left|\hat{\rho}(\boldsymbol{\omega}')\right|^2 d\omega_1'\right]d\theta_j \leq \int_A\left[\sqrt{\int\frac{1}{(\omega_1')^2}\tilde{R}^2(\omega_1')d\omega_1'}\int\left|\omega_1'\right|\left|\hat{\rho}(\boldsymbol{\omega}')\right|^2 d\omega_1'\right]d\theta_j = \sqrt{\int\frac{1}{(\omega_1')^2}\tilde{R}^2(\omega_1')d\omega_1'}\int_A\int\left|\omega_1'\right|\left|\hat{\rho}(\boldsymbol{\omega}')\right|^2 d\boldsymbol{\omega}'. \tag{87}$$

Computing the first integral in (87), we get

$$\int\frac{1}{(\omega_1')^2}\tilde{R}^2(\omega_1')d\omega_1' = \frac{2}{\cos^2\phi}\int_{\frac{\omega_c'-B/2}{c_0}\cos\phi}^{\frac{\omega_c'+B/2}{c_0}\cos\phi}\frac{1}{(\omega_1')^2}d\omega_1' = \frac{2c_0}{\cos^3\phi}\left(\frac{1}{\omega_c'-B/2}-\frac{1}{\omega_c'+B/2}\right) = \frac{2Bc_0}{\cos^3\phi((\omega_c')^2-(B/2)^2)}. \tag{88}$$

Consider the second integral in (87). Since the integrand is strictly positive, from the θ_j integration we have

$$\int_A\int\left|\omega_1'\right|\left|\hat{\rho}(\boldsymbol{\omega}')\right|^2 d\boldsymbol{\omega}' \leq \int_{2\pi}\int\left|\omega_1'\right|\left|\hat{\rho}(\boldsymbol{\omega}')\right|^2 d\boldsymbol{\omega}'. \tag{89}$$

We now make the following change of variables

$$\cos\theta_j\omega_1' = \omega_1'', \;\; \sin\theta_j\omega_1' = \omega_2''. \tag{90}$$

Computing the Jacobian, we get

$$J = \frac{1}{|\omega_1'(\boldsymbol{\omega}'')|} = \frac{1}{\sqrt{(\omega_1'')^2+(\omega_2'')^2}}. \tag{91}$$

Thus, setting $\boldsymbol{\omega}'' = [\omega_1'', \omega_2'']$, the upper bound in (89) becomes

$$\int\left|\omega_1'\right|\left|\hat{\rho}(\boldsymbol{\omega}')\right|^2 d\boldsymbol{\omega}' = \int\left|\hat{\rho}(\boldsymbol{\omega}'')\right|^2 d\boldsymbol{\omega}'' = 4\pi^2\|\boldsymbol{\rho}\|^2, \tag{92}$$

where the last identity follows from Parseval's theorem. Hence, we obtain the upper bound on our integral approximation, i.e., the first term in (86) as

$$\int\tilde{R}(\omega_1')\left|\hat{\rho}(\boldsymbol{\omega}')\right|^2\boldsymbol{\omega}' \leq \frac{4\pi^2\|\boldsymbol{\rho}\|^2\sqrt{2Bc_0}}{(\cos\phi)^{3/2}\sqrt{(\omega_c')^2-(B/2)^2}} \approx \frac{4\pi^2\|\boldsymbol{\rho}\|^2\sqrt{2Bc_0}}{\omega_c'(\cos\phi)^{3/2}}. \tag{93}$$

We next evaluate the error term of the integral approximation in (92). Namely, the midpoint Riemann-sum approximation error is upper bounded as

$$|E_R| \leq Q\frac{A^3}{24\,N^2} \tag{94}$$

where Q is defined as

$$Q = \max_\theta\left|\frac{\partial^2}{\partial\theta^2}\int_{\left|\frac{\omega_c-B/2}{c_0}\cos\phi\right|}^{\left|\frac{\omega_c+B/2}{c_0}\cos\phi\right|}\left|\hat{\rho}(\boldsymbol{\omega}')\right|^2 d\omega_1'\right| \tag{95}$$

using the definition of $\tilde{R}(\omega_1')$.

Since the integrand is the squared absolute value of the Fourier transform of the reflectivity function evaluated at frequencies $\boldsymbol{\omega}'$, (95) can equivalently be written as

$$Q = \max_\theta\left|\sum_{l,l'}\frac{\partial^2}{\partial\theta^2}\tilde{f}(\theta,\boldsymbol{x}_l,\boldsymbol{x}_{l'})\tilde{\rho}(\boldsymbol{x}_l,\boldsymbol{x}_{l'})\right| \tag{96}$$

which is the form of a Frobenius inner product, where

$$\tilde{f}(\theta,\boldsymbol{x}_l,\boldsymbol{x}_{l'}) := \int_{\left|\frac{\omega_c-B/2}{c_0}\cos\phi\right|}^{\left|\frac{\omega_c+B/2}{c_0}\cos\phi\right|}\mathrm{e}^{-\mathrm{i}\boldsymbol{\omega}'\cdot(\boldsymbol{x}_l-\boldsymbol{x}_{l'})}d\omega_1'. \tag{97}$$

Observe that Q has an upper bound that only depends on the ℓ_2 norm of the underlying scene as

$$Q \leq \max_\theta\|\frac{\partial^2}{\partial\theta^2}\tilde{\mathbf{f}}\|_F\|\boldsymbol{\rho}\|^2, \tag{98}$$

and that $\max_\theta\|\frac{\partial^2}{\partial\theta^2}\tilde{\mathbf{f}}\|_F$ has only dependence on the imaging system, hence yields a universal upper bound for any scene reflectivity function in the specific imaging geometry. Evaluating

the integral in (97) and having $\omega_c \gg B$, $\tilde{f}$ can be approximated under the narrow-band assumption as

$$\tilde{f} \approx \frac{B}{c_0}\mathrm{sinc}\left(\frac{\omega_c}{c_0}\gamma(\theta)\cdot(\boldsymbol{x}_l-\boldsymbol{x}_{l'})\right). \tag{99}$$

Denoting $z=\frac{\omega_c}{c_0}\gamma(\theta)\cdot(\boldsymbol{x}_l-\boldsymbol{x}_{l'})$, the second order derivative of each component in $\tilde{f}$ with respect to θ is obtained as

$$\frac{\partial^2 z}{\partial\theta^2}\left(\frac{\cos z}{z}-\frac{\sin z}{z^2}\right) + \left(\frac{\partial z}{\partial\theta}\right)^2\left(-\frac{\sin z}{z}-\frac{2\cos z}{z^2}+\frac{2\sin z}{z^3}\right) \tag{100}$$

where

$$\begin{aligned}\frac{\partial^2 z}{\partial\theta^2} &= -\frac{\omega_c}{c_0}[\cos\theta,\sin\theta]^T\cdot(\boldsymbol{x}_l-\boldsymbol{x}_{l'}),\left(\frac{\partial z}{\partial\theta}\right)^2\\ &= \left(\frac{\omega_c}{c_0}\right)^2([-\sin\theta,\cos\theta]^T\cdot(\boldsymbol{x}_l-\boldsymbol{x}_{l'}))^2.\end{aligned} \tag{101}$$

By definition, the amplitude of sinc-function derivatives in (100) have a decay rate of $1/z$, whereas z and its derivatives in (100) grow with an order of the scene dimension L, as $\mathcal{O}(\frac{\omega_c}{c_0}L)$. Hence, evaluating the squared integral for the Frobenius norm, the growth is at a maximal order of $\mathcal{O}((\frac{\omega_c}{c_0})^3 L^3)$. We thereby obtain a final approximate upper bound on the universal constant Q as

$$\left|\frac{\partial^2}{\partial\theta^2}\int_{\left|\frac{\omega_c-B/2}{c_0}\cos\phi\right|}^{\left|\frac{\omega_c+B/2}{c_0}\cos\phi\right|}\hat{\rho}(\omega(\cos\theta+1),\omega\sin\theta)d\omega\right| \leq \mathcal{O}\left(\frac{B}{c_0}\left(\frac{\omega_c}{c_0}\right)^{\frac{3}{2}}L^{\frac{3}{2}}\right)\|\boldsymbol{\rho}\|^2. \tag{102}$$

Putting the terms derived in (102) and (93) into (85) and (76), we have

$$\delta \leq \frac{c_0}{B}\frac{K}{L}\sqrt{\frac{2\pi}{L}}\frac{1}{A}\left(\frac{4\pi^2\sqrt{2Bc_0}}{\omega_c'(\cos\phi)^{3/2}} + \mathcal{O}\left(\frac{B}{c_0}\left(\frac{\omega_c}{c_0}\right)^{\frac{3}{2}}L^{\frac{3}{2}}\frac{A^3}{N^2}\right)\right) \tag{103}$$

for the definition of δ in Definition 1, using the fact that $\|\boldsymbol{\rho}\|^4 = \|\tilde{\boldsymbol{\rho}}\|_F^2$ for the rank-1, PSD element $\tilde{\boldsymbol{\rho}}=\boldsymbol{\rho}\boldsymbol{\rho}^H$.

Re-organizing the terms using (26) and (28) defined in the statement of Theorem 1, and the fact that

$$\frac{K}{L\sqrt{L}}=\frac{\sqrt{L}}{\Delta^2}, \tag{104}$$

we finally obtain

$$\delta \leq \frac{2\pi}{A}\frac{2\lambda_c\sqrt{L\Delta_{\mathrm{res}}}}{\Delta^2(\cos\phi)^{3/2}}+\mathcal{O}\left(\frac{K}{(N/A)^2}\lambda_c^{-3/2}\right), \tag{105}$$

which completes the proof.

REFERENCES

[1] B. Yonel and B. Yazici, "A generalization of wirtinger flow for exact interferometric inversion," *SIAM J. Imaging Sci.*, vol. 12, no. 4, pp. 2119–2164, 2019.

[2] E. J. Candes, X. Li, and M. Soltanolkotabi, "Phase retrieval via Wirtinger flow: Theory and algorithms," *IEEE Trans. Inf. Theory*, vol. 61, no. 4, pp. 1985–2007, Apr. 2015.

[3] E. J. Candes, Y. Eldar, T. Strohmer, and V. Voroninski, "Phase retrieval via matrix completion," *SIAM J. Imag. Sci.*, vol. 6, no. 1, pp. 199–225, 2013.

[4] E. J. Candes and T. Strohmer, "Phaselift: Exact and stable recovery from magnitude measurements via convex programming," *Commun. Pure Appl. Math.*, vol. 66, no. 8, pp. 1241–1274, Aug. 2013.

[5] O. M. Bucci and G. Franceschetti, "On the spatial bandwidth of scattered fields," *IEEE Trans. Antennas Propaga.*, vol. 35, no. 12, pp. 1445–1455, Dec. 1987.

[6] O. M. Bucci and G. Franceschetti, "On the degrees of freedom of scattered fields," *IEEE Trans. Antennas Propag.*, vol. 37, no. 7, pp. 918–926, Jul. 1989.

[7] C. E. Yarman and B. Yazici, "Synthetic aperture hitchhiker imaging," *IEEE Trans. Image Process.*, vol. 17, no. 11, pp. 2156–2173, Nov. 2008.

[8] J. Garnier and G. Papanicolaou, "Passive sensor imaging using cross correlations of noisy signals in a scattering medium," *SIAM J. Imag. Sci.*, vol. 2, no. 2, pp. 396–437, 2009.

[9] L. Wang, I.-Y. Son, and B. Yazici, "Passive imaging using distributed apertures in multiple-scattering environments," *IOP Inverse Problems J.*, vol. 26, no. 6, pp. 1–37, Jun. 2010.

[10] H. Ammari, J. Garnier, and W. Jing, "Passive array correlation-based imaging in a random waveguide," *Multiscale Model. Simul.*, vol. 11, no. 2, pp. 656–681, 2013.

[11] E. Mason, I.-Y. Son, and B. Yazıcı, "Passive synthetic aperture radar imaging using low-rank matrix recovery methods," *IEEE J. Sel. Topics Signal Process.*, vol. 9, no. 8, pp. 1570–1582, Dec. 2015.

[12] J. Garnier, "Imaging in randomly layered media by cross-correlating noisy signals," *Multiscale Model. Simul.*, vol. 4, no. 2, pp. 610–640, 2005.

[13] O. I. Lobkis and R. L. Weaver, "On the emergence of the Green's function in the correlations of a diffuse field," *J. Acoust. Soc. Amer.*, vol. 110, no. 6, pp. 3011–3017, 2001.

[14] L. Borcea, G. Papanicolaou, and C. Tsogka, "Theory and applications of time reversal and interferometric imaging," *Inverse Problems*, vol. 19, no. 6, 2003, Art. no. S139.

[15] L. Borcea, G. Papanicolaou, and C. Tsogka, "Interferometric array imaging in clutter," *Inverse Problems*, vol. 21, no. 4, 2005, Art. no. 1419.

[16] L. Borcea, G. Papanicolaou, and C. Tsogka, "Coherent interferometric imaging in clutter," *Geophysics*, vol. 71, no. 4, pp. SI165–SI175, 2006.

[17] P. Blomgren, G. Papanicolaou, and H. Zhao, "Super-resolution in time-reversal acoustics," *J. Acoust. Soc. Amer.*, vol. 111, no. 1, pp. 230–248, 2002.

[18] P. T. Gough and M. A. Miller, "Displaced ping imaging autofocus for a multi-hydrophone SAS," *IEE Proc. Radar, Sonar Navig.*, vol. 151, no. 3, pp. 163–170, Jun. 2004.

[19] S. W. Flax and M. O'Donnell, "Phase-aberration correction using signals from point reflectors and diffuse scatterers: Basic principles," *IEEE Trans. Ultrason., Ferroelectr., Freq. Control*, vol. 35, no. 6, pp. 758–767, Nov. 1988.

[20] E. Mason and B. Yazici, "Robustness of LRMR based passive radar imaging to phase errors," in *Proc. EUSAR: 11th Eur. Conf. Synthetic Aperture Radar*, 2016, pp. 1–4.

[21] R. Novikov, "Formulas for phase recovering from phaseless scattering data at fixed frequency," *Bulletin des Sci. Mathématiques*, vol. 139, no. 8, pp. 923–936, 2015.

[22] P. Bardsley and F. G. Vasquez, "Kirchhoff migration without phases," *Inverse Problems*, vol. 32, no. 10, 2016, Art. no. 105006.

[23] Z. Chen and G. Huang, "Phaseless imaging by reverse time migration: Acoustic waves," *Numer. Math. Theory, Methods Appl.*, vol. 10, no. 1, pp. 1–21, 2017.

[24] A. Novikov, M. Moscoso, and G. Papanicolaou, "Illumination strategies for intensity-only imaging," *SIAM J. Imag. Sci.*, vol. 8, no. 3, pp. 1547–1573, 2015.

[25] J. Laviada, A. Arboleya-Arboleya, Y. Alvarez-Lopez, C. Garcia-Gonzalez, and F. Las-Heras, "Phaseless synthetic aperture radar with efficient sampling for broadband near-field imaging: Theory and validation," *IEEE Trans. Antennas Propag.*, vol. 63, no. 2, pp. 573–584, Feb. 2015.

[26] L. Wang, C. E. Yarman, and B. Yazici, "Doppler-Hitchhiker: A novel passive synthetic aperture radar using ultranarrowband sources of opportunity," *IEEE Trans. Geosci. Remote Sens.*, vol. 49, no. 10, pp. 3521–3537, Oct. 2011.

[27] L. Wang and B. Yazici, "Passive imaging of moving targets exploiting multiple scattering using sparse distributed apertures," *IOP Inverse Problems J.*, vol. 28, no. 12, pp. 1–36, Dec. 2012.
[28] L. Wang and B. Yazici, "Passive imaging of moving targets using sparse distributed apertures," *SIAM J. Imag. Sci.*, vol. 5, no. 3, pp. 769–808, 2012.
[29] S. Wacks and B. Yazici, "Passive synthetic aperture hitchhiker imaging of ground moving targets - I: Image formation and velocity estimation," *IEEE Trans. Image Process.*, vol. 23, no. 6, pp. 2487–2500, Jun. 2014.
[30] D. Kissinger, "Radar fundamentals," in *Proc. Millimeter-Wave Receiver Concepts 77 GHz Automot. Radar Silicon-Germanium Technol.*, 2012, pp. 9–19.
[31] L. Demanet and V. Jugnon, "Convex recovery from interferometric measurements," *IEEE Trans. Comput. Imag.*, vol. 3, no. 2, pp. 282–295, Jun. 2017.
[32] I. Waldspurger, A. d'Aspremont, and S. Mallat, "Phase recovery, maxcut and complex semidefinite programming," *Math. Program.*, vol. 149, no. 1/2, pp. 47–81, Feb. 2015.
[33] A. Chai, M. Moscoso, and G. Papanicolaou, "Array imaging using intensity-only measurements," *IOP Inverse Problems J.*, vol. 27, no. 1, pp. 1–16, Jan. 2011.
[34] B. Recht, M. Fazel, and P. Parrilo, "Guaranteed minimum-rank solutions of linear matrix equations via nuclear norm minimization," *SIAM Rev.*, vol. 52, no. 3, pp. 471–501, 2010.
[35] A. M. Haimovich, R. S. Blum, and L. J. Cimini, "Mimo radar with widely separated antennas," *IEEE Signal Process. Mag.*, vol. 25, no. 1, pp. 116–129, Jan. 2008.
[36] V. S. Chernyak, *Fundamentals of Multisite Radar Systems: Multistatic Radars and Multistatic Radar Systems*. New York, NY, USA: Gordon & Breach, 1998.
[37] H. Lev-Ari and A. J. Devancy, "The time-reversal technique re-interpreted: subspace-based signal processing for multi-static target location," in *Proc. IEEE Sensor Array Multichannel Signal Process. Workshop. (Cat. No.00EX410)*, Mar. 2000, pp. 509–513.
[38] L. Griffiths and C. Jim, "An alternative approach to linearly constrained adaptive beamforming," *IEEE Trans. Antennas Propag.*, vol. 30, no. 1, pp. 27–34, Jan. 1982.
[39] C. Prada and M. Fink, "Eigenmodes of the time reversal operator: A solution to selective focusing in multiple-target media," *Wave Motion*, vol. 20, no. 2, pp. 151–163, 1994.
[40] A. Paulraj, B. Ottersten, R. Roy, A. Swindlehurst, G. Xu, and T. Kailath, "Subspace methods for directions-of-arrival estimation," in *Handbook of Statistics*. New York, NY, USA: Elsevier, 1993, vol. 10, pp. 693–739.
[41] A. Kirsch, "Characterization of the shape of a scattering obstacle using the spectral data of the far field operator," *Inverse Problems*, vol. 14, no. 6, pp. 1489–1512, Dec. 1998.
[42] A. Kirsch and S. Ritter, "A linear sampling method for inverse scattering from an open arc," *Inverse Problems*, vol. 16, no. 1, pp. 89–105, Jan. 2000.
[43] T. Arens and A. Lechleiter, "The linear sampling method revisited," *J. Integral Equ. Appl.*, vol. 21, no. 2, pp. 179–202, Summer 2009.
[44] D. Strong and T. Chan, "Edge-preserving and scale-dependent properties of total variation regularization," *Inverse problems*, vol. 19, no. 6, 2003, Art. no. S165.
[45] Y. Yu, A. P. Petropulu, and H. V. Poor, "Mimo radar using compressive sampling," *IEEE J. Sel. Topics Signal Process.*, vol. 4, no. 1, pp. 146–163, Feb. 2010.
[46] M. A. Herman and T. Strohmer, "High-resolution radar via compressed sensing," *IEEE Trans. Signal Process.*, vol. 57, no. 6, pp. 2275–2284, Jun. 2009.
[47] K.-T. Kim, D.-K. Seo, and H.-T. Kim, "Efficient radar target recognition using the music algorithm and invariant features," *IEEE Trans. Antennas Propag.*, vol. 50, no. 3, pp. 325–337, Mar. 2002.
[48] L. Audibert and H. Haddar, "The generalized linear sampling method for limited aperture measurements," *SIAM J. Imag. Sci.*, vol. 10, no. 2, pp. 845–870, 2017.
[49] I. Catapano, L. Crocco, and T. Isernia, "Improved sampling methods for shape reconstruction of 3-D buried targets," *IEEE Trans. Geosci. Remote Sens.*, vol. 46, no. 10, pp. 3265–3273, Oct. 2008.
[50] L. Di Donato and L. Crocco, "Model-based quantitative cross-borehole GPR imaging via virtual experiments," *IEEE Trans. Geosci. Remote Sens.*, vol. 53, no. 8, pp. 4178–4185, Aug. 2015.
[51] M. Bevacqua, L. Crocco, L. D. Donato, T. Isernia, and R. Palmeri, "Exploiting sparsity and field conditioning in subsurface microwave imaging of nonweak buried targets," *Radio Sci.*, vol. 51, no. 4, pp. 301–310, 2016.
[52] M. Cheney and B. Borden, *Fundamentals of Radar Imaging*. Philadelphia, PA, USA: Siam, 2009, vol. 79.
[53] Y. Chen and E. J. Candes, "Solving random quadratic systems of equations is nearly as easy as solving linear systems," *Commun. Pure Appl. Math.*, vol. 70, pp. 0822–0883, 2017.
[54] B. Yonel, E. Mason, and B. Yazici, "Phaseless passive synthetic aperture radar imaging via wirtinger flow," in *Proc. IEEE 52nd Asilomar Conf. Signals, Syst. Comput.*, 2018, pp. 1623–1627.
[55] W. Rudin, *Real and Complex Analysis*, 3rd ed., New York, NY, USA: McGraw-Hill, 1987.

Bariscan Yonel (Student Member, IEEE) received the B.Sc degree in electrical engineering from Koc University, Istanbul, Turkey, in 2015. He is currently working toward the Ph.D. degree in electrical engineering with Rensselaer Polytechnic Institut, Troy, NY, USA. His research and thesis work focus on identifying and establishing the theoretical conditions of exact inversion from quadratic equations and their fundamental limits for wave-based imaging problems, using computationally efficient non-convex algorithms.

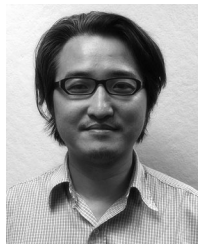

Il-Young Son received the B.Sc, M.Sc, and Ph.D. degrees in electrical engineering from Rensselaer Polytechnic Institute (RPI), Troy, NY, USA, in 2001, 2006, and 2018, respectively. His M.Sc. thesis was on Diffuse Optical Tomography and Functional NIR imaging while the topic of the Ph.D. thesis was on the application of polarimetry in passive radar imaging. After receiving his doctorate, he was a Postdoctoral Researcher with RPI in 2019, where he conducted research on autofocus techniques for SAR imaging and interferometric multistatic passive radar, incorporating real data processing to both areas. His research interests include passive radar imaging, radar polarimetry, and application of optimization techniques to radar data processing.

Birsen Yazici (Senior Member, IEEE) received the B.S. degrees in electrical engineering and mathematics from Bogazici University, Istanbul Turkey, in 1988, and the M.S. and Ph.D. degrees in mathematics and electrical engineering from Purdue University, West Lafayette, IN, USA, in 1990 and 1994, respectively. From September 1994 to 2000, she was a Research Engineer with General Electric Company Global Research Center, Schenectady NY, USA. During her tenure in industry, she worked on radar, transportation, industrial and medical imaging systems. From 2001 to June 2003, she was an Assistant Professor with the Department of Electrical and Computer Engineering, Drexel University. In Fall 2003, she joined Rensselaer Polytechnic Institute where she is currently a Full Professor with the Department of Electrical, Computer and Systems Engineering and with the Department of Biomedical Engineering. Her research interests include statistical signal processing, inverse problems in imaging, image reconstruction, biomedical optics, radar and X-ray imaging. She was an Associate Editor for the IEEE TRANSACTIONS ON IMAGE PROCESSING from 2008 to 2012, and for SIAM Journal on Imaging Science from 2010 to 2014. She is currently an Associate Editor for IEEE TRANSACTIONS ON GEOSCIENCES AND REMOTE SENSING. She is the recipient of the Rensselaer Polytechnic Institute 2007 and 2013 School of Engineering Research Excellence Awards. She holds 11 U.S. patents.